

The Origin of the Virgo Stellar Substructure

Jeffrey L. Carlin^{1,4}, William Yam¹, Dana I. Casetti-Dinescu², Benjamin A. Willett¹, Heidi J. Newberg¹,
Steven R. Majewski³, & Terrence M. Girard²

ABSTRACT

We present three-dimensional space velocities of stars selected to be consistent with membership in the Virgo stellar substructure. Candidates were selected from SA 103, a single $40' \times 40'$ field from our proper motion (PM) survey in Kapteyn's Selected Areas (SAs), based on the PMs, SDSS photometry, and follow-up spectroscopy of 215 stars. The signature of the Virgo substructure is clear in the SDSS color-magnitude diagram (CMD) centered on SA 103, and 16 stars are identified that have high Galactocentric-frame radial velocities ($V_{\text{GSR}} > 50 \text{ km s}^{-1}$) and lie near the CMD locus of Virgo. The implied distance to the Virgo substructure from the candidates is $14 \pm 3 \text{ kpc}$. We derive mean kinematics from these 16 stars, finding a radial velocity $V_{\text{GSR}} = 153 \pm 22 \text{ km s}^{-1}$ and proper motions $(\mu_{\alpha} \cos \delta, \mu_{\delta}) = (-5.24, -0.91) \pm (0.43, 0.46) \text{ mas yr}^{-1}$. From the mean kinematics of these members, we determine that the Virgo progenitor was on an eccentric ($e \sim 0.8$) orbit that recently passed near the Galactic center (pericentric distance $R_p \sim 6 \text{ kpc}$). This destructive orbit is consistent with the idea that the substructure(s) in Virgo originated in the tidal disruption of a Milky Way satellite. N -body simulations suggest that the entire cloud-like Virgo substructure (encompassing the “Virgo Overdensity” and the “Virgo Stellar Stream”) is likely the tidal debris remnant from a recently-disrupted massive ($\sim 10^9 M_{\odot}$) dwarf galaxy. The model also suggests that some other known stellar overdensities in the Milky Way halo (e.g., the Pisces Overdensity and debris near NGC 2419 and SEGUE 1) are explained by the disruption of the Virgo progenitor.

Subject headings: Galaxy:structure – Galaxy: kinematics and dynamics – Galaxy: stellar content – Proper motions – stars: kinematics and dynamics – galaxies: dwarf

¹Department of Physics, Applied Physics, and Astronomy, Rensselaer Polytechnic Institute, 110 8th Street, Troy, NY 12180, USA (carlij@rpi.edu)

²Astronomy Department, Yale University, P.O. Box 208101, New Haven, CT 06520-8101

³Department of Astronomy, University of Virginia, P.O. Box 400325, Charlottesville, VA 22904-4325

⁴Visiting Astronomer, Kitt Peak National Observatory and Cerro Tololo Inter-American Observatory, National Optical Astronomy Observatory, which are operated by the Association of Universities for Research in Astronomy (AURA) under cooperative agreement with the National Science Foundation.

1. Introduction

Galaxy formation is currently thought to proceed via the hierarchical merging of numerous smaller substructures, which are assimilated into the host galaxies by tidal disruption and, ultimately, dissolved (e.g., Johnston 1998; Abadi et al. 2003; Bullock & Johnston 2005; Font et al. 2006). This is by no means a new idea, as it was suggested by Searle & Zinn (1978) that late infall after the collapse of the initial protogalaxy was responsible for the apparent age spread among Milky Way (MW) globular clusters, and later (by, e.g., Majewski 1993; Majewski et al. 1996) that the build-up of the Galactic halo proceeds via agglomeration of dwarf galaxies. We have now seen this process in action via the numerous stellar tidal streams that have been discovered coursing through the MW’s halo (see Grillmair 2010 for a summary) and various other stellar substructures in the form of “clouds” of stars (the properties of known structures are summarized in Rocha-Pinto 2010). In the era of large-area, deep photometric and spectroscopic surveys, we are now entering the regime where not only narrow, kinematically-cold stellar streams can be found, but also the clouds and shells of debris seen in, e.g., the Johnston et al. (2008) models of hierarchical formation of Milky Way-like galaxies. The menagerie of morphological structures predicted by these models are now being seen with deep imaging around external galaxies (e.g., Chonis et al. 2011; Martínez-Delgado et al. 2010). Because of our perspective within the Galaxy, such features are more difficult to see in context and characterize. However, a look at the variety of morphological types of known structures discussed in Rocha-Pinto (2010) shows that large photometric surveys have begun finding the predicted remnants of halo assembly. The kinematical characterization of the clouds and shells that is needed to assess their origins and discern the nature of their progenitors has been more elusive, since identification of stellar members of such low surface-brightness features is difficult, and derivation of proper motions for such distant structures is challenging. The particular one of these apparent cloud-like stellar structures upon which we focus this work is the overdensity (or, perhaps, collection of stellar excesses) in the constellation Virgo.

The first recognition of a stellar overdensity in the halo near the Virgo constellation was the finding by Vivas et al. (2001) of a cluster of 5 RR Lyrae stars within $195^\circ < \text{RA} \lesssim 200^\circ$, at a distance of ~ 20 kpc in the first 100 deg^2 results from the QUEST survey. Shortly thereafter, Newberg et al. (2002) used F-type turnoff starcounts on the celestial equator to identify stellar overdensities, including one at $180^\circ < \text{RA} < 195^\circ$, $\text{Dec} = 0^\circ$ that was dubbed S297+63-20.0 (the naming scheme denotes that the feature is at $(l, b) \sim (297^\circ, +63^\circ)$ with turnoff magnitude $g \sim 20$). This feature, which is near the same region of sky as the Vivas et al. (2001) RR Lyrae, shows a clear main sequence extending downward from $g \sim 19$, corresponding to a distance (assuming an old, metal-poor population) of ~ 20 kpc. Since the distance is also similar to that of the Vivas et al. (2001) stars, this large-area overdensity might be associated with the RR Lyrae. Newberg et al. (2002) also noted that the color of the turnoff stars in S297+63-20.0 is intermediate between that of Sagittarius tidal debris and the typical MW halo turnoff, suggesting that the Virgo feature is related to neither of those structures.

Further results from the QUEST survey, which studied a 2.3-degree wide strip centered at $\text{Dec} \sim -1^\circ$, were presented in Vivas & Zinn (2003). In the 380 deg^2 portion of the QUEST survey discussed, the authors find 497 RR Lyrae between 4-50 kpc. Many of the distant RR Lyrae are Sgr debris, but the authors identify a distinct clump at mean magnitude of $\langle V_0 \rangle = 16.9 \pm 0.2$, corresponding to a distance of ~ 19 kpc. Because

of its location at $\langle RA \rangle \sim 186^\circ$, this grouping was dubbed the “12.4-hour clump”. Based on the RR Lyrae periods and period-amplitude distributions, it appears that the clump contains RR Lyrae of both Oosterhoff classes, making them more typical of dwarf galaxy populations than globular clusters. This 12.4-hour clump is within the same region and at the same distance as S297+63-20.0, which suggests an association. A “fluff” of overdensity was also seen in the Majewski et al. (2003) study of 2MASS-selected M-giant stars at the same position ($150^\circ < RA < 210^\circ$) as S297+63-20.0 and the 12.4-hour clump, though it was suggested by those authors to be part of the “descending, foreshortened loop” of the Sagittarius leading tidal tail. This idea was explored further by Martínez-Delgado et al. (2004), who developed a model of the Sgr disruption that produced debris at roughly the distance, position, and velocity of the Vivas & Zinn (2003) RR Lyrae and the Newberg et al. (2002) main sequence detections.

The first spectroscopic study of any of these overdensities came when Duffau et al. (2006) observed 18 RR Lyrae from the QUEST survey. Their study found that a clump of stars centered at $\alpha \sim 186^\circ (\pm 5^\circ)$ and $R_{\text{Sun}} = 19.6$ kpc is also clustered in velocity. The six stars making up this clump have a mean $\langle V_{\text{GSR}} \rangle = 99.8$ km s $^{-1}$, and a dispersion of 17.3 km s $^{-1}$. This clump of stars was dubbed the “Virgo Stellar Stream (VSS)”. Duffau et al. then expanded the sample to a larger area and RVs within $\sim 3\sigma$ of the peak, and identified 13 stars with $\langle V_{\text{GSR}} \rangle = 85$ km s $^{-1}$ with $\sim 25 - 30$ km s $^{-1}$ dispersion. These stars are spread over a distance range from $R_{\text{Sun}} = 16 - 20$ kpc (with one at ~ 24 kpc); thus, the VSS must be large and diffuse (or contain multiple overdensities). The metallicity of the 7 RRAb stars selected to be members is $\langle [\text{Fe}/\text{H}] \rangle = -1.86$, with $\sigma_{[\text{Fe}/\text{H}]} = 0.4$. The large spread in conjunction with the lack of an obvious intermediate-age population in the SDSS CMDs is taken as evidence of a low-luminosity, old, metal-poor dwarf galaxy progenitor for the VSS.

Further detections of halo overdensities from the QUEST RR Lyrae survey’s first catalog were presented by Vivas & Zinn (2006), who found that after removing the contribution of their best-fitting smooth halo model, the Virgo structure is visible as a peak at $RA \sim 186^\circ$ at a distance of ~ 17 kpc (spanning 12-20 kpc between $175^\circ < RA < 205^\circ$). Velocity substructures were seen among bright ($V < 16.1$) QUEST RR Lyrae by Vivas et al. (2008), including a grouping at $10.5 < D < 12$ kpc with $\langle V_{\text{GSR}} \rangle = 215$ km s $^{-1}$ and 25 km s $^{-1}$ dispersion (plus some stars at slightly lower velocities that may also be associated with the structure). These stars extend the Virgo substructure to more nearby distances than previously known. The mean metallicity of six of these bright RR Lyrae is $\langle [\text{Fe}/\text{H}] \rangle = -1.55$, with $\sigma_{[\text{Fe}/\text{H}]} = 0.15$ dex. Further spectroscopic data of QUEST RR Lyrae was reported by Duffau et al. (2010). This study found a VSS grouping with 23 members, having a mean RV of $\langle V_{\text{GSR}} \rangle = 129$ km s $^{-1}$. There are additional stars in a group at higher ($200 \lesssim V_{\text{GSR}} \lesssim 250$ km s $^{-1}$) velocity, but slightly more nearby (9-15 kpc). These, together with the 10-12 kpc ~ 200 km s $^{-1}$ stars from Vivas et al. (2008) suggest a velocity gradient with distance in the VSS region.

Table 1: Previous detections of stellar overdensities in Virgo.

source	RA (degrees)	Dec (degrees)	distance (kpc)	V_{GSR} (km s ⁻¹)	[Fe/H] (dex)	notes
Vivas et al. (2001)	[195,200]	[-2.3,0]	~ 20	5 QUEST RR Lyrae
Newberg et al. (2002)	190.2	0.3	~ 20	SDSS F-turnoff stars
Vivas & Zinn (2003)	186	-1	19	QUEST RR Lyrae ("12.4-hour clump")
Duffau et al. (2006)	[175,205]	[-2.5,0.0]	[16,20]	99.8	-1.86	spectra of QUEST RR Lyrae ("Virgo Stellar Stream")
Vivas & Zinn (2006)	189	-0.8	17 ([12,20])	QUEST RR Lyrae
Newberg et al. (2007)	191.2, 185.6	-7.8, -0.1	18	130±10	...	SDSS F-turnoff stars
Juric et al. (2008)	[160,210]	[-5,15]	6-20	...	$\lesssim -1.0$	SDSS "tomography" ("Virgo Overdensity")
Keller et al. (2008)	[180,230]	[-12,-2]	[16,19]	SEKBO RR Lyrae
Vivas et al. (2008)	[170,210]	[-2.3,0.0]	[8,12]	215	-1.55	spectra of bright ($V < 16.1$) QUEST RR Lyrae
Keller et al. (2009)	[180,210]	[-15,0]	[17,20]	SEKBO RR Lyrae with SDSS photometry
Prior et al. (2009)	[170,210]	[-14,0]	[16,22]	127 ± 10 ^a	-1.95 ± 0.1	spectra of SEKBO RR Lyrae
Brink et al. (2010)	185.9	-1.0	...	137 ^b	...	spectroscopy WFC on INT 2.5-meter
Duffau et al. (2010)	[180,210]	[-4,0]	[7,21]	129	...	"VSS" group of QUEST RR Lyrae
Duffau et al. (2010)	[180,210]	[-4,0]	[7,18]	~ 220	...	higher-velocity group of QUEST RR Lyrae
Keller (2010)	[180,210]	[-2,6]	[12,18]	SDSS subgiants
Casey et al. (2012)	[180,194]	[-3,0]	~ 20	~ 130	-2.0	spectra; Feature B
Casey et al. (2012)	[180,194]	[-3,0]	~ 20	~ 220	-1.2	spectra; Feature C

Values in brackets represent ranges in which those particular studies found Virgo substructure members.

^aNote that this study contained some stars at high ($V_{\text{GSR}} > 180$ km s⁻¹) velocity that were not identified by the authors as VSS members.

^bWe note that the authors' estimate of $V_{\text{GSR}} = 137$ km s⁻¹ uses only stars with $V_{\text{GSR}} < 170$ km s⁻¹; using all stars with $100 < V_{\text{GSR}} < 350$ km s⁻¹ yields a median $V_{\text{GSR}} = 152$ km s⁻¹.

The overdensity of RR Lyrae in Virgo has also been studied by the SEKBO survey, which spans $\sim 10^\circ$ about the ecliptic. Keller et al. (2008) show that the Virgo overdensity is visible among SEKBO RR Lyrae at $R \sim 20$ kpc between $180^\circ < RA < 230^\circ$. Photometric and spectroscopic follow-up of SEKBO stars by Prior et al. (2009) uncovered a handful of additional VSS stars between 16-22 kpc at mean $V_{\text{GSR}} = 127 \pm 10$ km s $^{-1}$ and dispersion of ~ 27 km s $^{-1}$. These stars have $\langle [\text{Fe}/\text{H}] \rangle = -1.95 \pm 0.1$, with scatter of 0.4 dex (note that an additional star at $V_{\text{GSR}} = 193$ km s $^{-1}$ and $[\text{Fe}/\text{H}] = -1.34$ was not included as a member in their sample). Prior et al. (2009) also calculate a number density of excess stars and use this to find that in a ~ 760 deg 2 area centered on $(\alpha, \delta) = (186^\circ, -4^\circ)$ the total luminosity is $M_V = -11.9$ (or $M_V = -10.1$ using values more closely resembling the Jurić et al. 2008 distances). The authors claim that because VSS stars have been found between 12-24 kpc with a large metallicity spread, we must be looking at the remains of a disrupted dwarf spheroidal galaxy. We also note that this study extended the VSS to much lower latitudes of $b \sim 45^\circ$ ($\delta \sim -15^\circ$).

An extensive examination of the Virgo substructure was enabled by SDSS Data Release 5 (DR5) data. Newberg et al. (2007) studied Virgo using SDSS starcounts of BHB stars, blue stragglers, and F-turnoff stars as well as SEGUE radial velocities of F-type turnoff stars in the region of the Virgo overdensity. The authors showed using BHB stars and blue stragglers within 15 kpc of the Sgr orbital plane that Sgr debris in this region does not pass through the position of S297+63-20.5 identified by Newberg et al. (2002), ruling out the association of the Virgo structure with leading-arm Sgr debris. Since the SDSS footprint by DR5 covered the entire north Galactic cap (NGC), Newberg et al. were able to make starcount maps of the NGC using photometrically-selected F-turnoff stars. These maps showed that the Virgo (S297+63-20.5) structure is prominent mostly at magnitudes $20 < g < 21$, spanning at least $\sim 15^\circ$ across. Newberg et al. (2007) use SEGUE radial velocities of F-turnoff stars in two plates at $(l, b) = (300^\circ, 55^\circ)$ and $(288^\circ, 62^\circ)$ to search for a Virgo RV signature. A clear excess of F stars is seen at $\langle V_{\text{GSR}} \rangle = 130 \pm 10$ km s $^{-1}$ with stars in the 30 km s $^{-1}$ wide bins adjacent to the peak, suggesting a large velocity dispersion within the structure.

Brink et al. (2010) undertook a spectroscopic survey of 111 faint ($18.0 < g_0 < 21.8$), blue ($-0.1 < (g-r)_0 < 0.65$) turnoff candidates centered on the VSS, the majority of which seem to be Sagittarius leading arm stars. However, there is a broad peak at $\langle V_{\text{GSR}} \rangle = 137$ km s $^{-1}$ with dispersion 22 km s $^{-1}$ that is consistent with the Newberg et al. (2007) VSS/VOD detections from F-turnoff stars. We note also that the mean and dispersion quoted by Brink et al. (2010) was measured using only stars between $105 < V_{\text{GSR}} < 170$ km s $^{-1}$, but there is a long tail of stars at higher velocities in their sample.

The final spectroscopic study we mention is that of Casey et al. (2012). These authors observed a sample of 178 K-giant stars in four separate fields between $180 < RA < 195^\circ$ and $-3 < Dec < 0^\circ$. In addition to a clear signal from the Sagittarius tidal tail at $V_{\text{GSR}} < 0$ km s $^{-1}$, they found a significant excess of high-velocity ($V_{\text{GSR}} \gtrsim 70$ km s $^{-1}$) stars. The authors suggest that these ~ 20 -kpc-distant stars may be two separate features (denoted “Feature B” and “Feature C”) with $70 \lesssim V_{\text{GSR}} \lesssim 250$ km s $^{-1}$.

Another SDSS study by Jurić et al. (2008) explored the photometric properties of the overdensity in Virgo. The prominent factor of ~ 2 stellar excess spanning over 1000 deg 2 in this study was dubbed the “Virgo overdensity (VOD)” by the authors. The VOD extends from the lower limit of the SDSS footprint

at $Z \sim 6$ kpc above the Galactic plane to the outer limit of their study at $Z \sim 20$ kpc, suggesting that it may extend even farther. The feature appears to narrow at higher Z , which suggests that it may extend further into (or beyond) the plane. Assuming a distance of 10 kpc and 1000 deg^2 area, Jurić et al. (2008) estimated a lower limit on the total luminosity of $L_r = 0.1 \times 10^6 L_\odot$, or $M_r = -7.8$. The color-color distribution of VOD stars suggests that the VOD is more metal-poor than the thick disk. However, Juric et al. (as well as Majewski et al. 2003 previously) see the VOD in 2MASS-selected M giants, so there must also be a relatively metal-rich population associated with the VOD as well. Again, because of its low surface brightness, large extent, well-defined outline, and low metallicity, the authors argue that the VOD is the result of a low-metallicity dwarf galaxy merging with the Milky Way.

Additional work using SDSS-derived photometric metallicity estimates by An et al. (2009) explored the entire NGC region. The VOD in the region between $270^\circ < l < 330^\circ$ and $60^\circ < b < 70^\circ$ was found by these authors to have median metallicity of $[\text{Fe}/\text{H}] = -2.0 \pm 0.1$. Note, however, that this is for *all* dwarf stars in this region, only some of which are VOD members. An et al. claim that the fact that the median $[\text{Fe}/\text{H}]$ derived is the same as the halo metallicity in the symmetric area of the sky means that the additional VOD stars are halo-like.

Using SDSS photometrically-selected sub-giants, Keller (2010) mapped the north Galactic cap, and resolved the VOD into a number of discrete overdensities of smaller area than that of Jurić et al. (2008). Keller et al. (2009) found a similar result using combined SEKBO RR Lyrae data and SDSS photometry. The VOD appears to break up into at least three distinct clumps in that study. This may suggest significant inhomogeneity across the larger $\sim 1000 \text{ deg}^2$ feature of Jurić et al. (2008).

A summary of the numerous detections of stellar overdensities in Virgo discussed in this section is given in Table 1. From this table, it is obvious that there is a large complex of structures in this part of the sky detected using a variety of stellar tracers, that (based on their similar distances and velocities) may be related to each other. Each of the surveys presents a data set limited either in its spatial coverage or based on a modest-sized sample of spectra, making interpretation difficult.

Understanding the nature of the Virgo overdensities¹ and their possible inter-relationship will ultimately require measurement of the kinematics and/or chemistry of large numbers of stars in the large area where overdensities have been detected. In contrast, we focus on a small region of sky, but where we can take advantage of precise measurements of three-dimensional kinematics of selected Virgo candidates. This study is a follow-up to that of Casetti-Dinescu et al. (2009; hereafter CD09), which presented the orbit of a single RR Lyrae consistent with membership in a Virgo substructure. This star had radial velocity measurements from SDSS and proper motion measurements from photographic plate data derived from the survey of Kapteyn’s Selected Areas described initially by Casetti-Dinescu et al. (2006). The 3-D kinematics of this particular star place it (and, by inference, the substructure of which it is part) on a highly eccentric orbit, having just passed its pericenter. The authors considered possible positional associations with Milky

¹Because the relationship between the various structures including the “Virgo Overdensity (VOD)” and “Virgo Stellar Stream (VSS)” in the Virgo region is unclear, we will simply refer to “the Virgo stellar (sub)structure” throughout this work. We will show later in this work that all of these structures are likely related, making this semantic approach reasonable.

Way satellites beyond Galactic radii of 50 kpc, and found that the unusual globular cluster NGC 2419 is within 13 kpc of the derived orbit.

The present study revisits the result of CD09 using spectra for additional stars from the same proper-motion catalog used in the CD09 study. We spectroscopically identify 16 Virgo members, from which we derive mean proper motions and RVs. From these, we derive an orbit for the Virgo substructure, and use this orbit to produce N -body models based on the measured kinematics. The paper is structured as follows: In Section 2 we discuss the data used for this study, which include proper motions from the Selected Areas survey, SDSS photometry, and low-resolution spectroscopy obtained on three separate observing runs. Section 3 outlines the methods we used to select Virgo substructure members, and compares our data sets to SDSS data from the surrounding regions of sky. The criteria adopted to identify Virgo structure members were based on radial velocity, color-magnitude location, proper motion, and to some extent metallicity, yielding a final sample of 16 Virgo members. We follow this, in Section 4, with analysis of the kinematics derived from the identified members. We derive an orbit based on the mean motion we measure, and use this to generate an N -body simulation that roughly reproduces the (still poorly-known) characteristics of the Virgo substructure(s). In Section 5, we search for positional and kinematical associations of known Milky Way satellites and substructures with our derived orbit for Virgo debris, and discuss a few possible associations. In particular, our data and subsequent simulations suggest plausible associations of the Virgo debris with NGC 2419, the Pisces Overdensity, the Newberg et al. (2003) 90-kpc “Sgr debris”, and a stellar overdensity in the field of view of the ultrafaint dwarf galaxy SEGUE 1. We conclude by arguing that we have convincingly shown that all or most of the known Virgo overdensities are plausibly part of a single disrupted dwarf galaxy, and that a number of other Milky Way substructures may be associated with this same progenitor.

2. The Data

2.1. Photometry and Proper Motions

Proper motions used in this study come from the survey described in Casetti-Dinescu et al. (2006, hereafter CD06); we provide a brief introduction here, and refer the reader to CD06 for details. The survey consists of ~ 50 fields of $40' \times 40'$ spaced ~ 15 degrees apart in strips along the celestial equator (i.e., $\delta = 0^\circ$) and $\delta = \pm 15^\circ$ (see Fig. 1 in CD06 for a map). These fields are the “Selected Areas (SAs)” designated by Kapteyn (1906) for his proposed comprehensive study of the Milky Way. The particular field of view in this study, SA 103, was also the focus of a previous publication (CD09). SA 103 is centered at $(\alpha, \delta)_{2000} = (178.765^\circ, -0.562^\circ)$, or $(l, b) = (274.56^\circ, 59.17^\circ)$. The photographic plates making up our earliest epoch for proper motions were originally taken between 1909-1912 (analysis of photometry from these plates appears in Seares et al. 1930) as part of the Kapteyn survey at the Mt. Wilson 60-inch. Matching plates (in field of view, depth, and plate scale) were taken by S. Majewski between 1996-1998 at the Las Campanas du Pont 2.5-meter telescope to provide a ~ 90 -year baseline for measurement of proper motions. The Mt. Wilson 60-inch plates have plate scale $27''12 \text{ mm}^{-1}$, and the plate scale for du Pont 2.5-meter data is

$10.''92 \text{ mm}^{-1}$, with both having a field of view of $40' \times 40'$. All of these plates were digitized using the Yale PDS microdensitometer. The data were supplemented by intermediate-epoch plates from the Palomar Observatory Sky Survey (POSS-I), taken in the early 1950s, to extend the limiting magnitude of our proper motions beyond the depth provided by the Mt. Wilson plates. Proper motions were measured by comparing the positions of objects on 1 Mt. Wilson plate, 4 POSS-I plates, and 2 du Pont plates. Each of the Mt. Wilson and du Pont plates contain a long and short exposure offset spatially, providing 2 measurements per plate. Two separate scans of the POSS-I plates were analyzed; one from the PMM measuring engine at USNO, and the other from the PDS microdensitometer at STScI. Thus there is a total of 14 possible measurements from the 7 plates in SA 103. The correction from relative to absolute proper motions was done using four QSOs and 302 background galaxies in the field of view (see CD09 for details), from which we derived zero points of $\mu_\alpha \cos \delta = 3.89 \pm 0.27 \text{ mas yr}^{-1}$ and $\mu_\delta = 2.31 \pm 0.30 \text{ mas yr}^{-1}$; these were applied to the data to place the proper motions in an absolute frame.² QSOs are taken from SDSS QSO catalogs, and galaxies are identified in the plate scans. Proper motion uncertainties range from $\sim 1 \text{ mas yr}^{-1}$ per star at the bright end (i.e., $g \lesssim 18$) to 2-3 mas yr^{-1} at the faint ($g \sim 20-21$), limiting magnitude of the plates.

Rather than relying on photographic photometry, we took advantage of the fact that high-quality photometry from SDSS DR7 was available for the SA 103 area. The photometric data we have used throughout this work are corrected for reddening and extinction (from Schlegel et al. 1998, the mean reddening is $E(B-V) = 0.026$ along this line of sight). By comparison of photometric catalogs to the much deeper SDSS data, we have found that the proper motion catalogs are 86% complete for point sources at $g = 20.0$, falling to 15% completeness at $g = 21.0$. The limiting magnitude set by the shallow Mt. Wilson plates (i.e., for stars with $\sim 90 \text{ yr}$ baseline) is $g \sim 20.0$, with 90% completeness at $g = 17.0$. A color magnitude diagram is given in the upper left panel of Figure 1 for all stars with measured proper motions in SA 103. For comparison, the middle panel shows the predictions of the Besançon Galaxy model (Robin et al. 2003) for the same field of view, and the right panel shows all stars from SDSS DR8 within the same field of view. In the DR8 panel, an upper main sequence is clearly visible, with a turnoff at $g \sim 19.0$, $g-r \sim 0.3$ – this likely corresponds to the MSTO of the Virgo structure identified by Newberg et al. (2002). The same feature is visible in our SA 103 data, and is not represented in the Besançon model, which bolsters our assertion that this turnoff is due to a substructure in the Milky Way halo. To further confirm that this turnoff structure is not expected among Galactic stellar populations in the SA 103 field of view, we compare SDSS data in SA 103 to SDSS CMDs at 90° intervals in longitude and approximately the same latitude ($b = 60^\circ$). Assuming the Milky Way has an axisymmetric stellar halo, these four high-latitude fields seen in Figure 1 should exhibit the same features among faint, blue halo stars. Indeed, the three fields at $l = 0^\circ, 90^\circ$, and 180° (the bottom panels in Figure 1) look similar to each other, but the SA 103 field of view (the upper right panel) shows a clear main sequence extending downward from $g \sim 19, g-r \sim 0.3$. Within the overplotted box at $0.15 < g-r < 0.5$ and $18.5 < g < 20.5$, there are a total of 93, 130, 85, and 183 stars for $l = 0, 90, 180, 274^\circ$ respectively. These correspond to fractions of 0.123, 0.125, 0.106, and 0.142 of the total number of stars above the dashed line (i.e., with $g < 0.7(g-r) + 20.8$) in each panel of Figure 1. We thus conclude that the apparent clumping of

²Note that these differ from the zero points in CD09, but are consistent within the errors, and thus make little difference in our final conclusions. The difference between the measurements is in the sample of QSOs used in the two, separate measurements.

stars at $g \gtrsim 18.5$ and $0.15 < g-r < 0.5$ in our SA 103 proper motion data near $l = 274^\circ$ is due to a significant stellar excess that is present along this line of sight. Based on these starcounts we surmise that $\gtrsim 30\%$ of the stars in this CMD-selection region are part of the Virgo substructure.

2.2. Radial Velocities

In Figure 1 there is no obvious red giant branch associated with the MSTO feature, meaning that spectroscopic follow-up aimed at efficiently identifying and measuring the kinematics of Virgo substructure members should ideally focus on the high-density turnoff region. However, many of the spectra we observed for this study were taken as backup targets during observing time scheduled for other projects. Thus the spectroscopic targets, shown as large colored circles in Figure 2, are not optimally selected and tend to sample brighter magnitudes. The box overplotted in Figure 2 ($0.15 < g-r < 0.5$, $18.5 < g < 20.5$; the same as in Figure 1) surrounds the apparent MSTO of the Virgo structure, and thus contains the best spectroscopic candidates. Of the total of 215 stars for which we obtained spectra, 53 are within this box, with the majority of the remaining spectra at brighter magnitudes. Many of the stars brighter than $g \sim 18.5$ were selected in the region immediately surrounding the RR Lyrae star ($g = 17.05$, $g-r = 0.24$) on which the CD09 study focused, with the hope of identifying additional AGB/HB stars in the Virgo structure. The remainder of bright targets are redward of the thin/thick disk MSTO, where Virgo RGB candidates would be expected to reside.

Spectra of candidates were obtained on three separate observing runs. The first of these, in June 2009, used the Hydra multifiber spectrograph on the WIYN 3.5-meter telescope.³ A single setup consisting of 70 targets was observed at $R \sim 1500$ (3.35 \AA at $\lambda = 5200 \text{ \AA}$) using the 600-line (“600@10.1”) grating centered at $\lambda \sim 5700 \text{ \AA}$ (providing wavelength coverage of $4300-7100 \text{ \AA}$). The remaining candidates were observed as backup targets during runs at Cerro Tololo Inter-American Observatory in February 2010 and January 2011 using the Hydra multifiber spectrograph on the 4-meter Blanco telescope. The observing time for these runs was granted by NOAO to search for QSOs to use as astrometric reference sources in the field of view of the Carina dwarf spheroidal – results from that study will be presented in a future work. We observed at low resolution ($R \sim 850$), using the KPGL2 grating in first order centered at $\lambda \sim 6000 \text{ \AA}$. This setup was chosen to provide spectra that cover a broad ($\lambda \approx 3400-8200 \text{ \AA}$) wavelength range for finding the emission lines for QSOs within a large redshift window. Such spectra are not ideal for stellar kinematics, providing radial velocities of $\sim 10-20 \text{ km s}^{-1}$ accuracy (compared to $5-10 \text{ km s}^{-1}$ with the WIYN+Hydra setup; both estimates assume cross-correlations accurate to $\sim \frac{1}{30}$ of a resolution element). However, in both the 2010 and 2011 runs, our observations were scheduled in a period when the Carina dSph was unobservable at the end of the night, so we observed SA 103 to fill extra time. In February 2010, we observed 3 configurations totaling 188 stars that had spectra of sufficient signal-to-noise ($S/N > 10$) to derive velocities. In January 2011 we observed two additional SA 103 configurations with the same spectrograph setup, totaling 162

³The WIYN Observatory is a joint facility of the University of Wisconsin-Madison, Indiana University, Yale University, and the National Optical Astronomy Observatory.

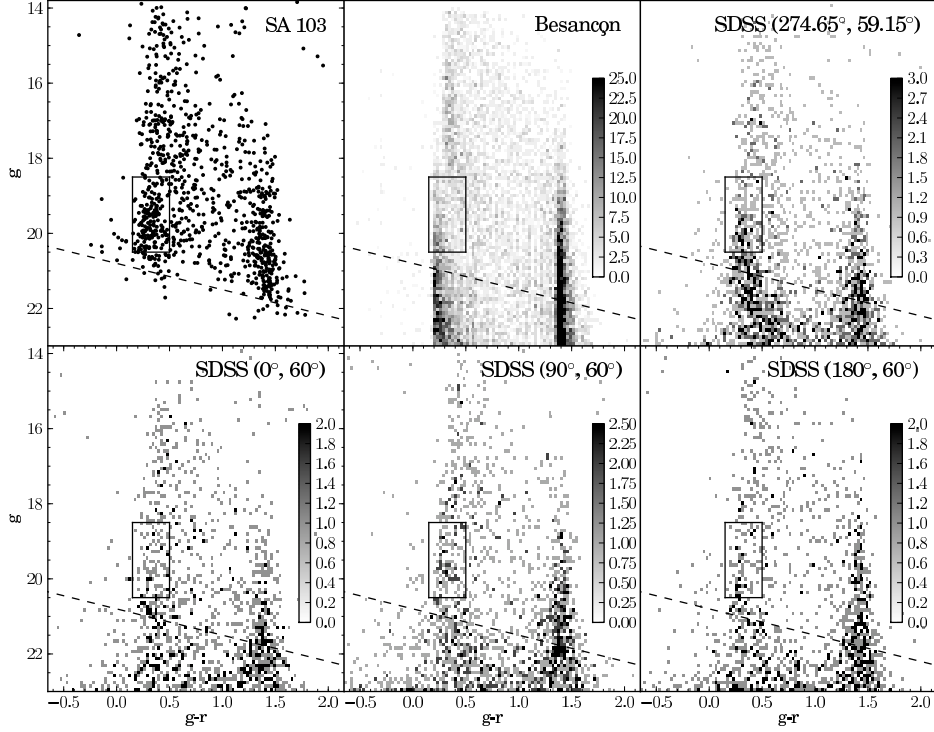


Fig. 1.— Color magnitude diagrams comparing all stars with measured proper motions in our SA 103 data (upper left panel) at $(l, b) = (274.6^\circ, 59.2^\circ)$ with output of the Besançon model along the same line of sight (upper middle panel) and SDSS CMDs from one-degree fields at $b \sim 60^\circ$ at $\sim 90^\circ$ intervals in Galactic longitude (the upper-right and lower three panels, with l, b as labeled; the upper right field is SDSS data within the SA 103 field of view). For SA 103 we show each individual star, while all of the other panels are binned Hess diagrams, with the grayscale density values given by the colorbar in each panel. The dashed line in each panel, defined by $g < 0.7(g-r) + 20.8$, roughly represents the magnitude limit of the SA 103 data, and is given for reference. Assuming the Galactic halo is spherically symmetric at such high latitudes, the starcounts of halo stars within the box overplotted on each panel should be roughly equal at each longitude. We find a total of 183 stars within the CMD-selection box in the upper-right panel (corresponding to SA 103), well above the totals of 93, 130, and 85 that are found in each of the fields at $l = 0, 90, 180^\circ$, respectively. When we instead consider the fraction of the total number of stars above the dashed line that are within the boxed region, we find 0.123, 0.125, 0.106, and 0.142 for $l = 0, 90, 180$, and 274° , respectively. We posit that this excess over the number of stars in symmetric fields (all selected from data of equal quality and depth) signals the presence of a significant overdensity (comprising $\sim 30\%$ of the stars in the boxed region) in SA 103.

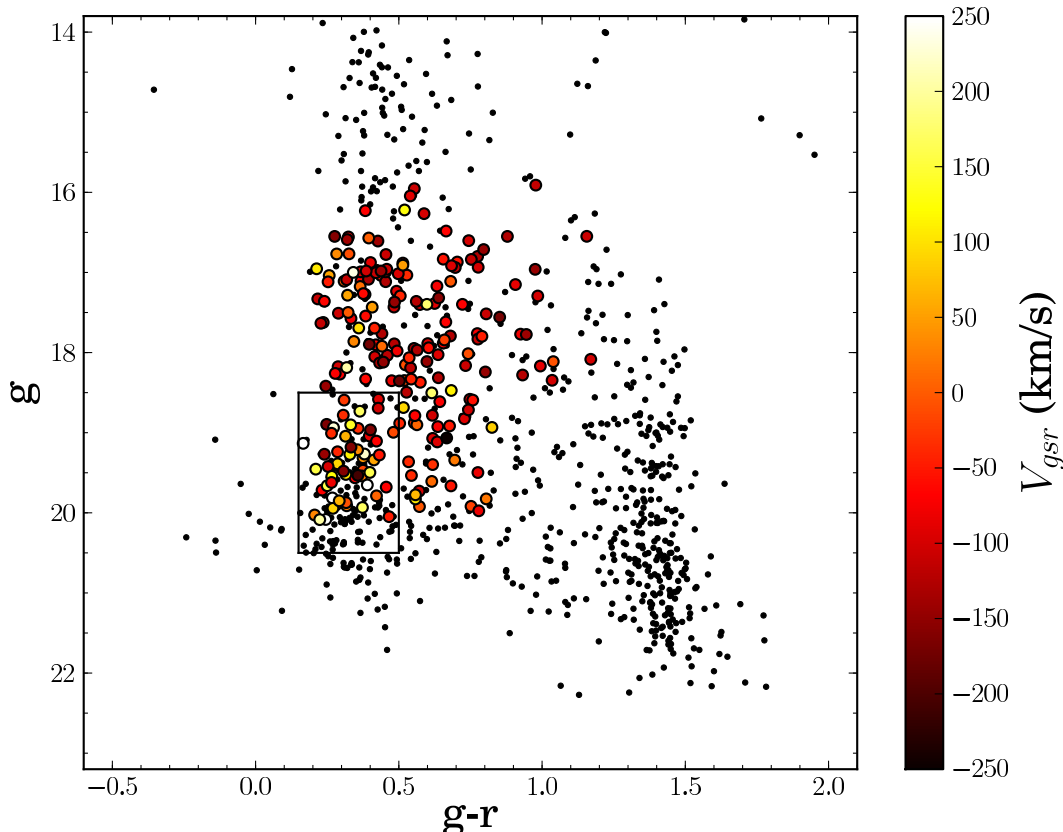


Fig. 2.— Color-magnitude diagram of all stars with measured proper motions in SA 103 shown as small black dots. Stars with spectroscopic data are highlighted by larger circles color-coded by V_{GSR} . Brighter colors correspond to higher V_{GSR} . The boxed region corresponds to the same Virgo turnoff selection area as in Figure 1. Note that a larger fraction of the light-colored (i.e., high-velocity) stars is present in the area of the Virgo turnoff than outside this box.

stars with usable spectra. Many stars were targeted on multiple configurations to allow cross-checking of the radial velocities; thus the total number of stars with measured velocities in SA 103 is 215.

For all observing, the target configurations were observed multiple times to enable cosmic-ray removal. The initial pre-processing of 2-D spectra used the CCDRED package in IRAF.⁴ One-dimensional spectra were extracted from the summed 2-D frames using the DOHYDRA routines (also in IRAF) for multifiber data reduction. Dispersion solutions were determined using 30-35 emission lines from arc lamp exposures

⁴IRAF is distributed by the National Optical Astronomy Observatory, which is operated by the Association of Universities for Research in Astronomy (AURA) under cooperative agreement with the National Science Foundation.

taken at each Hydra configuration. Bright radial velocity standards of various spectral types from F through K (both dwarfs and giants) were observed on each run. Each of these was observed through multiple fibers, to yield numerous cross-correlation spectra for RV measurement. Cross-correlation of these standard spectra against each other was done using the IRAF FXCOR package; we found that measured velocities of the RV standards typically agreed with published values to within $1\text{--}2\text{ km s}^{-1}$ for the June 2009 WIYN+Hydra run, and to $\lesssim 4\text{ km s}^{-1}$ for the lower-resolution Feb. 2010 and Jan. 2011 CTIO+Hydra observing. The radial velocities for program stars were then derived by cross-correlating the object spectra against all of the standard stars observed on the same run on which the target star was observed.

Radial velocity uncertainties were derived using the Vogt et al. (1995) method, as described in Muñoz et al. (2006) and Carlin et al. (2012). Because the Tonry-Davis ratio (TDR; Tonry & Davis 1979) scales with S/N , we were able to use the dependence of the TDR on S/N mapped via multiple observations of each standard star (which of course have varying S/N) to derive individual RV uncertainties from the measured TDR of each spectrum. Typical RV uncertainties for individual measurements are $\sigma_V \approx 10\text{--}20\text{ km s}^{-1}$ for spectra having $S/N \gtrsim 15\text{--}20$ per Angstrom. For the 100 stars (out of 215 total) that were observed multiple times, the final radial velocities represent the error-weighted mean values of individual measurements. We note that the RV uncertainties based on the TDR method may be underestimated; comparisons of the velocities of stars observed multiple times show standard deviations of $25\text{--}30\text{ km s}^{-1}$. As this includes all RV measurements (including those from low S/N spectra), we estimate that typical uncertainties are $\sim 20\text{ km s}^{-1}$.

2.3. Metallicities

To estimate metallicities from the low-resolution spectra used in this study, we relied on the well-calibrated Lick spectral indices (see, e.g., Worthey et al. 1994; Friel 1987). Details of the software pipeline produced by our group for this purpose will appear in a forthcoming paper (Carlin et al. 2012, *in prep.*). The program derives $[\text{Fe}/\text{H}]$ based on fits of the behavior of $[\text{Fe}/\text{H}]$ as a function of eight Lick Fe indices and the $\text{H}\beta$ index as defined by Worthey et al. (1994). The fits are calibrated using the known $[\text{Fe}/\text{H}]$ and spectral indices in the atlas of Schiavon (2007, based on the spectra of Jones 1998). This code has been shown to yield $[\text{Fe}/\text{H}]$ measurements of ~ 0.3 dex precision (or perhaps better) for low-resolution spectra having $S/N > 20$. For all stars with multiple measurements of $[\text{Fe}/\text{H}]$, we adopted the weighted mean from all measurements. Comparisons of $[\text{Fe}/\text{H}]$ for the stars with multiple observations show a standard deviation of ~ 0.3 dex in the residuals between individual observations, suggesting that this is a reasonable value for the typical metallicity uncertainty.

3. Virgo Substructure Candidate Selection

We have already shown in Section 2.1 that the stellar excess of blue, faint stars in SA 103 is not due to expected Galactic halo populations. Our estimate that $\sim 30\%$ of the stars within the CMD box

surrounding the turnoff region should be Virgo members suggests that roughly 15-20 of the 53 spectroscopic targets within that box should be part of the Virgo substructure, with a handful of additional RGB and AGB candidates at brighter magnitudes. Figure 2 shows the CMD for all stars with measured proper motions in SA 103, highlighting stars having spectra with $S/N > 10$. Stars are color coded by radial velocity to search for clumping in V_{GSR} . From these data, there appears to be a higher concentration of high velocity stars (the lighter colored points) in the boxed region of the CMD. This is consistent with prior studies claiming that the VSS is comprised of high velocity stars.

Figure 3 shows histograms of the line-of-sight V_{GSR} ⁵ of all stars in the SA 103 field; the left panel depicts all stars that have spectroscopic data with $S/N > 10$ (the color-coded points highlighted in Figure 2). In the right panel we show only a subset of faint, blue stars corresponding to the boxed turnoff region in Figures 1 and 2. In the absence of substructure, stars within this box will be primarily Galactic halo turnoff stars. These halo stars should have a velocity distribution centered at $V_{\text{GSR}} \sim 0 \text{ km s}^{-1}$. A Gaussian fit to all halo stars from the Besançon model for the SA 103 field yields a velocity dispersion for the halo of $\sim 90 \text{ km s}^{-1}$, which we overplot in the right panel as a reference. The histograms in each panel are compared to the aforementioned Besançon model (the dashed blue lines) corresponding to the same field. In the left panel, the model was normalized so that the number of stars in the velocity range $-300 < V_{\text{GSR}} < 100 \text{ km s}^{-1}$ is equal to the number of stars in the same range in SA 103. This velocity range was chosen so that the normalization includes only the region of the SA 103 data that is free from apparent substructure. In the right panel, the Besançon model counts were scaled by the fraction of the total number of stars in SA 103 within the CMD-selection box that were observed; i.e., because we obtained spectra of 53 of 183 total stars in the turnoff box (determined from SDSS DR8 data), the Besançon histogram was scaled down by a factor of 53/183. If the SA 103 data contained only halo stars, the Besançon model scaled in this manner should fairly accurately predict the total number of stars in the right panel of Figure 3; clearly there are more stars in SA 103 than predicted by the model. There seems to be an excess of stars in the region of $V_{\text{GSR}} \gtrsim 100 \text{ km s}^{-1}$ relative to both the Besançon model and the theoretical halo distribution. This excess appears to have a narrow peak centered at a value somewhat greater than the $\langle V_{\text{GSR}} \rangle = 137 \text{ km s}^{-1}$ found by Brink et al. (2010), though there also appear to be extra stars over a much broader range of high velocities. Note also that the peaks at $V_{\text{GSR}} \sim -75 \text{ km s}^{-1}$ and $\sim -170 \text{ km s}^{-1}$ seen by Newberg et al. (2007), Brink et al. (2010), and Casey et al. (2012) are apparent in this field of view; these peaks have been suggested to contain Sagittarius tidal debris.

To verify the existence of the apparent high-velocity excess, a comparison sample of all stars between $0.15 < g - r < 0.5$ and $18.5 < g < 20.5$ that were observed spectroscopically by SEGUE from $265^\circ < l < 283^\circ$ and $50^\circ < b < 68^\circ$ (i.e., a $> 300 \text{ deg}^2$ area surrounding SA 103) was extracted from SDSS DR8. A histogram of velocities for these stars is seen in Figure 4. Because of the prominence of the Sagittarius stream at negative V_{GSR} in this region, we show only $V_{\text{GSR}} > 0 \text{ km s}^{-1}$ in the figure. For comparison, we overlay (as a dashed, blue line) the Besançon distribution from the smaller SA 103 field, scaled so that the number of stars between $0 < V_{\text{GSR}} < 100 \text{ km s}^{-1}$ is equal to that in the SDSS histogram. There may be

⁵Velocity in the Galactic Standard of Rest, defined as $V_{\text{GSR}} = V_{\text{helio}} + 9.0 \cos b \cos l + 232.0 \cos b \sin l + 7.0 \sin b$.

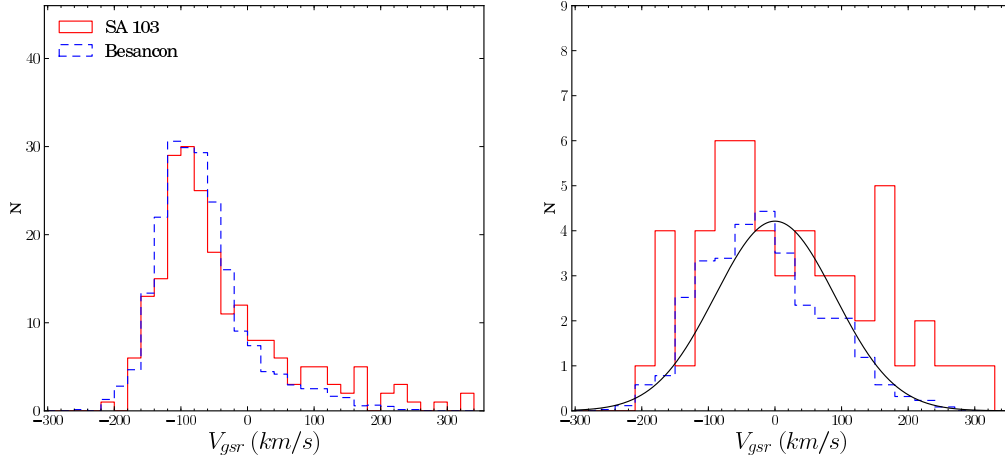


Fig. 3.— The left panel shows the measured V_{GSR} for all stars with spectroscopic data in SA 103 as the solid (red) histogram. The right panel contains only stars within the CMD box outlined in Figures 1 and 2. The blue dashed line in both panels represents the velocities predicted by the Besançon model in the field of SA 103 within the same color and magnitude ranges as the SA 103 stars. On the left, the Besançon distribution has been scaled such that the area under the histogram within the region between $-300 < V_{\text{GSR}} < 100 \text{ km s}^{-1}$ equals that of our SA 103 sample. On the right, the Besançon model is scaled by the fraction of the total number of stars within the CMD-selection box among SDSS DR8 data in this field of view that were observed; i.e., since we obtained spectra of 53 of 183 total stars, the Besançon histogram was scaled down by a factor of 53/183 to match the number of SA 103 stars observed spectroscopically. In the left panel, we include only stars between $16 < g < 20, 0.2 < g-r < 0.9$ from the Besançon model to roughly mimic the color and magnitude range covered by the SA 103 Hydra spectra. On the right, a Gaussian centered at $V_{\text{GSR}} = 0 \text{ km s}^{-1}$ with a $\sigma = 90 \text{ km s}^{-1}$ (representing the typical Galactic halo distribution, with $\sigma = 90 \text{ km s}^{-1}$ derived from a fit to the stars identified as halo members in the Besançon model) is also superposed, again normalized to the area of the SA 103 histogram within the region mentioned above. In the right panel (i.e., within the main sequence turnoff region contained by the CMD selection box) there is a clear excess of SA 103 stars over both the model and the halo predictions at $V_{\text{GSR}} \gtrsim 120 \text{ km s}^{-1}$. This excess is not confined to a narrow, kinematically-cold peak, but rather spreads over a large range in velocity. Note also that there may be stellar excesses present at $-100 \lesssim V_{\text{GSR}} \lesssim -50 \text{ km s}^{-1}$ and $V_{\text{GSR}} \sim -170 \text{ km s}^{-1}$; these correspond to similar excesses seen in this region of the sky by Newberg et al. (2007) and Brink et al. (2010) and suggested to be related to the Sagittarius tidal stream.

differences in the model between the smaller SA 103 field and the larger SDSS region, but such differences should be small because the expanded field is centered in SA 103. To represent expected Galactic halo populations, we also overplot a Gaussian centered at 0 km s^{-1} with a $\sigma = 90 \text{ km s}^{-1}$. As in our SA 103 data, the DR8 stars exhibit a clear excess in each histogram bin at high ($V_{\text{GSR}} \gtrsim 120 \text{ km s}^{-1}$) velocities relative to the model and the predicted halo distribution. Because the SEGUE selection function has a patchy

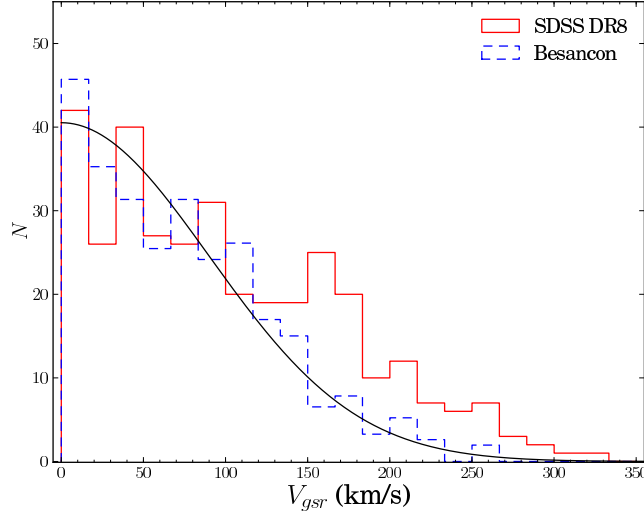


Fig. 4.— Galactic rest-frame radial velocities of stars selected from $265^\circ < l < 283^\circ$ and $50^\circ < b < 68^\circ$ from SDSS DR8 within the same CMD box (i.e, between $0.15 < g-r < 0.5$ and $18.5 < g < 20.5$) as in SA 103. The Besançon model from the 1 deg^2 field of SA 103 is shown as a dashed blue line for comparison. Here, the Besançon model was normalized so that the areas of the histograms are equal within the region of $0 < V_{\text{GSR}} < 100 \text{ km s}^{-1}$ (the data was cut off at $V_{\text{GSR}} > 0 \text{ km s}^{-1}$ because many Sagittarius stream stars appear in this region of sky at negative velocities). A Gaussian centered at 0 km s^{-1} with a dispersion of 90 km s^{-1} (representing the Milky Way halo) is plotted as a solid black line. There is a distinct excess of stars in every bin at $V_{\text{GSR}} \gtrsim 120 \text{ km s}^{-1}$ relative to both the Besançon predictions and the halo Gaussian.

distribution in color and magnitude, these stars are likely not a complete representation of the velocity distribution in this region. The excess of stars at high V_{GSR} is present even in this sample, leading us to conclude that (a) the apparent excess in SA 103 is due to a real overdensity at high ($V_{\text{GSR}} \gtrsim 120 \text{ km s}^{-1}$) velocities, and (b) the large spread of velocity in the excess is intrinsic, and not an artifact of the low resolution of our Hydra data.

Once a rough idea of the velocity of Virgo candidate stars was known, we proceeded with a detailed candidate selection. The steps we undertook to identify a sample of Virgo substructure members were:

1. Select all stars with $40 < V_{\text{GSR}} < 350 \text{ km s}^{-1}$. This broad range in velocity was chosen to include all Virgo substructure members, but will also contain some MW contaminants. A total of 38 stars were selected in this manner.
2. Narrow this sample to include only stars with at least 3 position measurements spanning at least a 40-yr time baseline to ensure that their proper motions are well-measured. In Figure 5, which compares proper motions of sample 1 in the left panel to those of the Besançon model on the right, there is

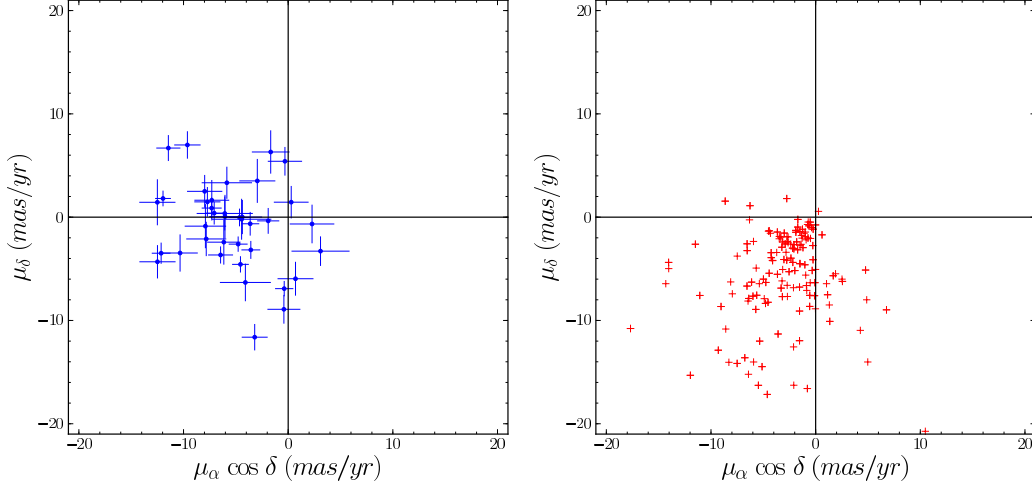


Fig. 5.— The left panel shows the proper motion vector point diagram (VPD) of all stars with well-measured PMs and $40 < V_{\text{GSR}} < 350 \text{ km s}^{-1}$ in SA 103. On the right we show stars from five realizations of the Besançon model within the same range of V_{GSR} as the left panel. Color and magnitude cuts from $16 < g_0 < 20$ and $0.25 < (g-r)_0 < 0.7$ were applied to the Besançon points since spectroscopic data from SA 103 are roughly limited to within this region. The SA 103 stars predominantly occupy a much different region than the predicted Galactic halo stars in this field. The mean proper motion of the stars in the velocity-selected SA 103 sample is $(\mu_\alpha \cos \delta, \mu_\delta) \sim (-5.2, 0.0) \text{ mas yr}^{-1}$.

a clear clumping of the proper motions about the median value of $(\mu_\alpha \cos \delta, \mu_\delta) = (-4.8, -0.2) \text{ mas yr}^{-1}$. Furthermore, this clump is clearly offset from the expected PMs of halo stars predicted by the Besançon model. We thus choose to keep only those stars with $\Delta\mu < 8 \text{ mas yr}^{-1}$, where $\Delta\mu$ is the offset from the median PMs of the stars in selection 1. This selection retains 30 stars.

3. Calculate the offset of each star in sample 2 from an appropriate color-magnitude sequence for the sample 2 stars. For this purpose we chose to use the empirical SDSS globular cluster ridgelines from An et al. (2008). This mitigates any uncertainties that would arise from the use of theoretical isochrones (see An et al. 2008 for illustration of the differences between empirical and theoretical ridgelines for MW clusters). Implicit in our use of globular cluster ridgelines is the assumption that the Virgo stars come from a predominantly old ($> 10 \text{ Gyr}$) stellar population; this is a reasonable assumption if the stars came from a dSph galaxy. The median metallicity of the 23 stars from sample 2 with spectra having $S/N > 15$ is $[\text{Fe}/\text{H}] \approx -1.1$ with $\sigma_{[\text{Fe}/\text{H}]} = 0.6$. We used the SDSS ($g, g-r$) ridgeline from An et al. (2008) for the globular cluster with metallicity nearest this value – that of M5, a cluster with $[\text{Fe}/\text{H}] = -1.27$. We plotted the dereddened CMD of all stars from SDSS DR8 in the SA 103 field of view (the stars that make up the upper-right panel of Figure 1), highlighting the candidates in sample 2. We then overplotted the M5 ridgeline, shifting it in distance until we visually determined a “best-fit” distance of $\sim 14 \text{ kpc}$. We excised all stars more than 0.2 magnitudes from

the 14-kpc M5 locus in $(g, g-r)$ at magnitudes fainter than $g = 17.5$; this selection criterion serves to remove stars well off the expected CMD locus based on the observed turnoff, and the magnitude limit means that this selection is only applied for the turnoff, subgiant branch, and lower RGB. The upper RGB and AGB are not included because these regions are much more sensitive to differences in the (unknown quantities) age and $[\text{Fe}/\text{H}]$. Although our derived metallicity is higher than most other estimates for Virgo-substructure stars, and the distance we have found is slightly nearer than most findings, this has little effect on the CMD filtering. A generous width of ± 0.2 magnitudes from the ridgeline would likely encompass all of the same stars if we were to change the parameters of the ridgeline used for filtering. This additional cut reduces the sample to 25 stars.

4. After selection number 3, the proper motions of most of the remaining stars were clumped tightly about $(\mu_\alpha \cos \delta, \mu_\delta) = (-5.1, -0.2)$, with some obvious outliers at the edges of the distribution. This is illustrated in Figure 6, which shows the proper motion vector point diagrams (VPDs) of all stars with $40 < V_{\text{GSR}} < 350 \text{ km s}^{-1}$ (i.e., sample 1) in the left panel, color-coded by their measured radial velocities. We noted that many of these stars in the outer regions of the PM distribution were also at the extreme ends of the V_{GSR} selection range, suggesting that they were Galactic interlopers, or had suspect proper motion measurements (typically having only 4-5 of the 14 possible position measurements). We thus chose to remove all stars with $\Delta\mu < 5 \text{ mas yr}^{-1}$ from sample 3, where the 5 mas yr^{-1} limit was chosen by examination of the left panel of Figure 6. The VPD of the remaining sample of 16 stars is shown in the right panel of Figure 6. None of the weighted mean proper motions and radial velocities of samples 3 and 4 varied more than 1σ from the sample 2 measurements, suggesting that the somewhat arbitrary choices of exclusion criteria were not subjectively biasing our selections strongly. This final sample of 16 stars is highlighted in the CMD in Figure 7. The CMD shows all stars in sample 3 as filled symbols, color-coded by radial velocity. The 16 Virgo candidates constituting sample 4 are filled circles, and stars excluded by the proper motion cut are triangles. The RR Lyrae star RR 167, a known VSS member from Casetti-Dinescu et al. (2009), is the cyan-colored circle at $g \sim 17, g-r \sim 0.2$, and the two stars with $V_{\text{GSR}} > 300 \text{ km s}^{-1}$ are shown as green filled hexagons. The overlaid isochrones from Girardi et al. (2004) are for 10 Gyr populations, with $[\text{Fe}/\text{H}] = -1.2$, and distances of 14, 17, and 20 kpc (spanning the range of most Virgo substructure detections from the literature). The 14 kpc isochrone appears to be the best match, and the 20 kpc ridgeline is clearly discrepant with the Virgo candidates.

We note that the final sample of 16 stars contains three stars at $g \sim 17, (g-r) < 0.4$ that, if they are members, must be horizontal branch stars (specifically, RR Lyrae). One of these three stars, known as RR 167, has already been shown by Casetti-Dinescu et al. (2009) to be a member of the VSS, so we believe that it is reasonable to include the other two in our sample. (Note that although these stars may not have been detected as RR Lyrae in the QUEST catalog of Vivas et al. (2004), the $\sim 70\%$ completeness of QUEST for RRc-type stars in this region of sky suggests that some bona fide RR Lyrae may have been missed by QUEST.) There are also two stars in the sample at rather high RVs of $V_{\text{GSR}} > 300 \text{ km s}^{-1}$, shown as filled green hexagons at $g = 19.75$ and $g = 19.91$; these two stars have proper motions consistent with membership, and because there is not a narrow peak in the RVs due to Virgo stars, we choose to retain them in our samples.

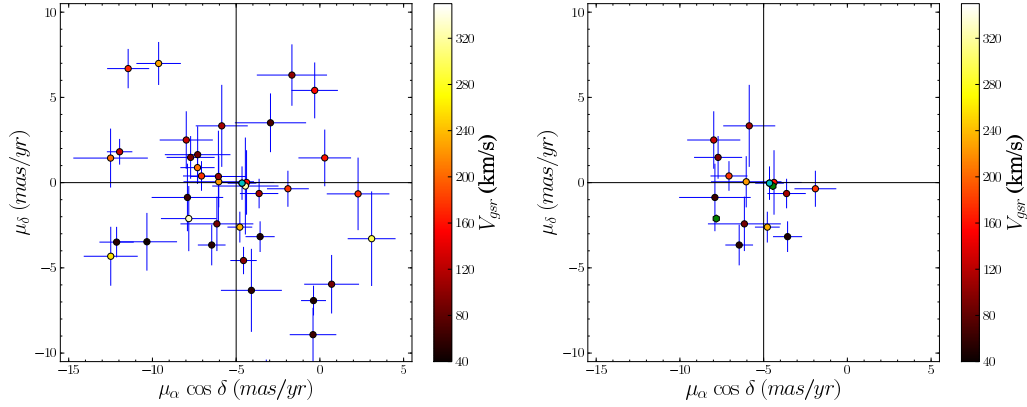


Fig. 6.— The panels show proper motions of Virgo substructure candidates color coded by V_{GSR} . The panels on the left show stars with $40 < V_{\text{GSR}} < 350 \text{ km s}^{-1}$, while the ones on the right show just the final selection. Again, RR 167 is highlighted in cyan.

However, these two high-velocity stars appear to lie below the MSTO of the 14-kpc isochrone, and thus may be more distant than the majority of the Virgo members. This may signify extension of the Virgo structure along the line of sight, including possibly a velocity gradient with distance.

Of the 16 stars in the “final” sample, 11 had spectra with $S/N > 20$, and all 16 had $S/N > 14$. From these, we derived metallicities with ~ 0.3 -dex precision; Figure 8 shows metallicities for all SA 103 stars with spectroscopic $S/N > 15$ as a function of velocity. The first selection of $40 < V_{\text{GSR}} < 350 \text{ km s}^{-1}$ Virgo candidates are highlighted with larger (red/green) symbols; large red circles are the final Virgo sample, the two green circles are the stars flagged in Figure 2 for having $V_{\text{GSR}} > 300 \text{ km s}^{-1}$, and the downward-facing triangles are stars removed from the final sample based on proper motion and CMD criteria. One star from the final sample does not appear in the figure because of what is likely a spurious $[\text{Fe}/\text{H}] = -3.75$. The 15 stars at $[\text{Fe}/\text{H}] > -3.5$ yield a mean value of $\langle [\text{Fe}/\text{H}] \rangle = -1.1 \pm 0.2$, with $\sigma_{[\text{Fe}/\text{H}]} = 0.7$ (note that this becomes $\langle [\text{Fe}/\text{H}] \rangle = -1.0 \pm 0.1$, $\sigma_{[\text{Fe}/\text{H}]} = 0.6$ if the single star at $[\text{Fe}/\text{H}] \sim -2.8$ is excluded). This metallicity for the Virgo candidates is consistent with that found from isochrone fitting, and more metal-poor than the predominantly thick-disk stars toward the left side (i.e., with $-150 < V_{\text{GSR}} < 50 \text{ km s}^{-1}$) of Figure 8.

4. Kinematics of Virgo Debris

Statistical kinematical information for the 16 identified Virgo substructure candidates is given in Table 2. Shown in the table are the mean spatial coordinates and error-weighted mean proper motions, radial velocities, and metallicities. The best fit kinematical parameters were converted from proper motion and radial velocity to right-handed Galactocentric Cartesian velocities using the method described in Johnson & Soderblom (1987). A Sun-Galactic center distance of 8.0 kpc was used, as well as solar velocity components in the Galactic rest frame of $(U, V, W) = (9, 232, 7) \text{ km s}^{-1}$. The resulting Galactic Cartesian

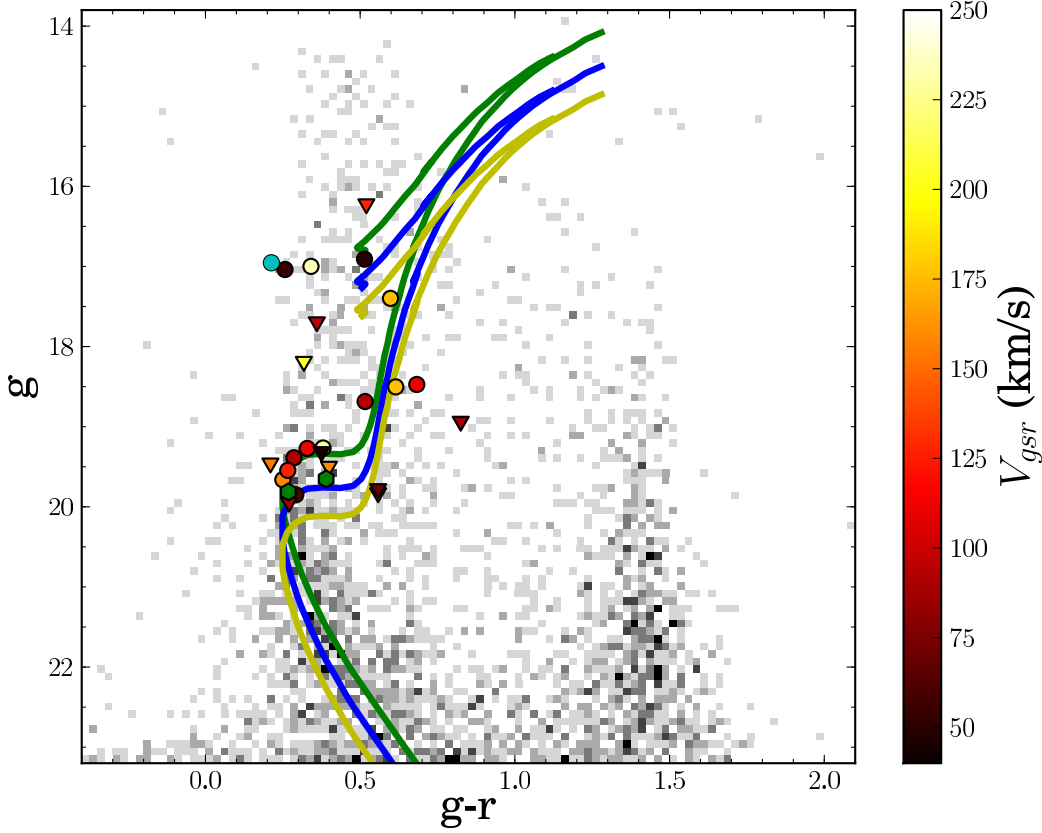


Fig. 7.— Dereddened color magnitude diagram of all stars with $40 < V_{\text{GSR}} < 350 \text{ km s}^{-1}$, $-12 < \mu_{\alpha} \cos \delta < 2 \text{ mas yr}^{-1}$, $-6 < \mu_{\delta} < 6 \text{ mas yr}^{-1}$, and measured on at least 3 photographic plates highlighted as circles and triangles. Symbols are color coded by the measured V_{GSR} . The greyscale Hess diagram in the background represents stars detected within the field using SDSS DR8 data. Isochrones of age 10 Gyr, metallicity $[\text{Fe}/\text{H}] = -1.2$, and distances 14, 17, and 20 kpc from Girardi et al. (2004) are superposed in green, blue, and yellow, respectively. Stars that were removed from the sample based on CMD position and proper motion are shown as triangles. The stars in the final selection are shown as filled circles. RR 167, an RR Lyrae star shown to be a VSS member (Casetti-Dinescu et al. 2009), is highlighted in cyan, and the two stars at high ($V_{\text{GSR}} > 300 \text{ km s}^{-1}$) velocities are filled green symbols.

velocity components of the Virgo debris are $(U, V, W) = (-264.1, -331.1, 123.9) \pm (65.7, 50.5, 33.0) \text{ km s}^{-1}$.

These best fit kinematic parameters were used to generate an orbital model. The Galactic gravitational potential adopted is that from Willett et al. (2009) (which is, in turn, based on Law et al. 2005): a three component potential that consists of a Miyamoto & Nagai (1975) disk, a Hernquist spheroid representing the bulge, and a logarithmic halo. The Galactic potential parameters are the same as those in Law et al.

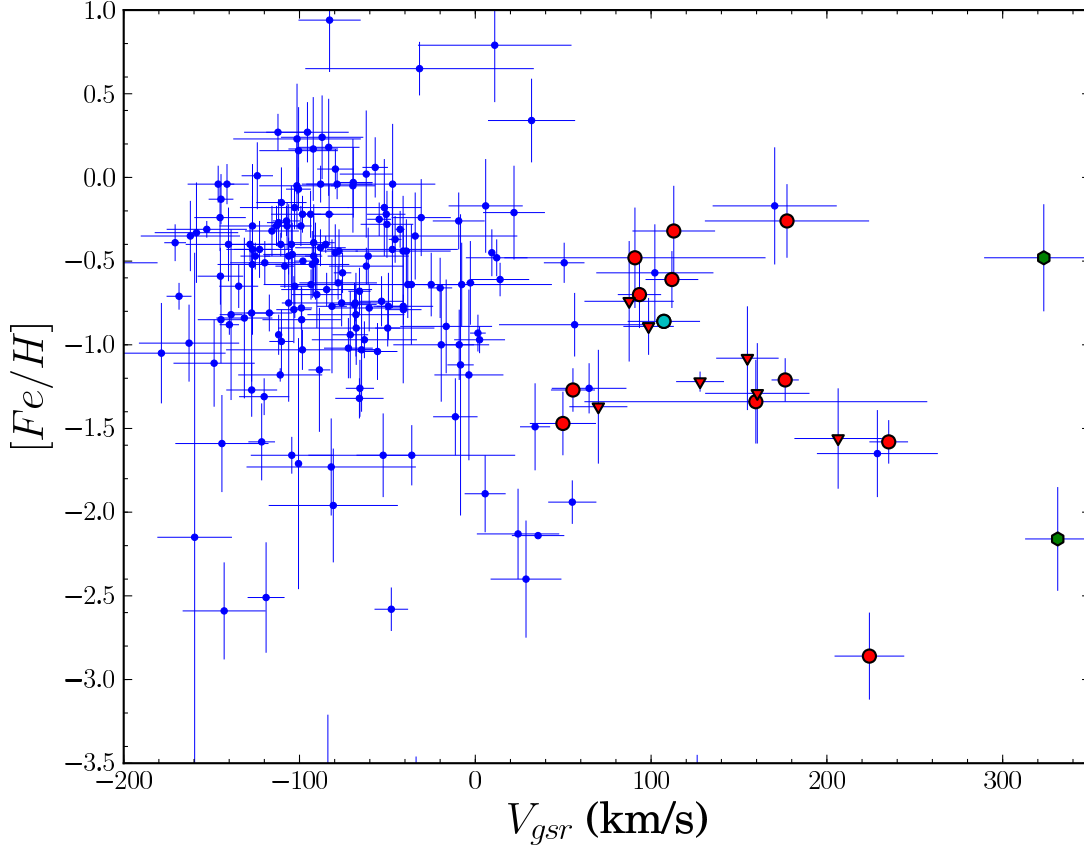


Fig. 8.— Metallicity ($[Fe/H]$) vs. V_{GSR} for all stars in our sample having spectra with $S/N > 15$. The majority of the stars between $-150 < V_{GSR} < 50 \text{ km s}^{-1}$ are likely MW thin/thick-disk stars with $[Fe/H] > -1.0$. The large filled circles and triangles are the stars in our initial Virgo-candidate velocity selection. Triangles are stars that were removed from the sample by subsequent selection criteria, leaving only the large filled circles as the final Virgo candidates. The two points at the far right side have been colored green to distinguish these $V_{GSR} > 300 \text{ km s}^{-1}$ stars from the rest of the sample (as in Figure 2). The mean metallicity of the final sample is $[Fe/H] = -1.1$.

(2005). Orbits were constructed using the mkorbit tool of the NEMO Stellar Dynamics Toolbox (Teuben 1995). The orbit was integrated for 3 Gyr both forward and backward using the values tabulated.

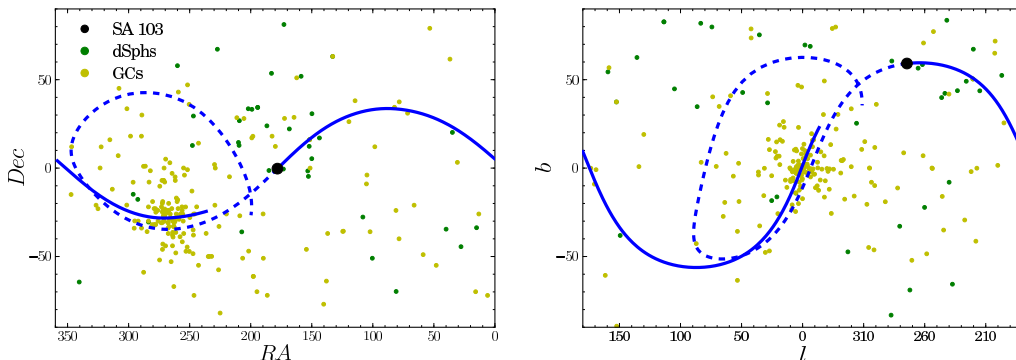


Fig. 9.— The orbit resulting from our measured Virgo kinematics, integrated for 1 Gyr forward and backward, is shown as the thick blue line in each of the panels above. The dashed portion is the backward integration (i.e., the path of the infalling progenitor), and the solid part represents the forward integration of the orbit. The left panel depicts the orbital path in equatorial coordinates, and the right panel in Galactic coordinates. The kinematics used to generate this orbit are given in Table 2. The location of SA 103 is shown as a large black dot at $(\alpha, \delta) = (178.7, -0.6)^\circ$, or $(l, b) = (274.6, 59.1)^\circ$. The positions of known globular clusters and dwarf galaxies are plotted in the background as yellow and green points respectively.

4.1. Orbit

Figure 9 shows the resulting orbit in both equatorial and Galactic coordinates. Milky Way dwarf spheroidal galaxies (dSphs) and globular clusters (GCs)⁶ are overplotted for later reference with respect to finding possible orbital associations and/or the progenitor. The orbit has apo- and peri-centers of $R_a = 52^{+87}_{-24}$ kpc and $R_p = 5.6^{+0.9}_{-0.8}$ kpc, with eccentricity $e \equiv (R_a - R_p)/(R_a + R_p) = 0.81^{+0.10}_{-0.27}$ (errors on these quantities are derived by propagating the uncertainties in the kinematics). The orbital inclination with respect to the Galactic plane is $i \equiv \arcsin(|z_{\max}|/R_{z\max}) = 54 \pm 3^\circ$, where $|z_{\max}|$ is the maximum height above or below the plane, and $R_{z\max}$ is the distance from the Galactic center where the orbit passes through $|z_{\max}|$. The orbital period (measured between successive apocenters) is $P_{\text{orb}} = 0.7^{+1.2}_{-0.3}$ Gyr. Plots of the orbit in distance and V_{GSR} vs. Galactic longitude are shown in Figure 10. Again the dwarf galaxies and globular clusters are plotted in the background for reference. The high eccentricity ($e \sim 0.8$) of this orbit is evident, with the satellite’s trajectory having just passed pericenter after swooping in from the outer halo.

The orbit was converted to Galactic right-handed Cartesian XYZ coordinates, with the convention that the Sun is centered at $(X, Y, Z) = (-8, 0, 0)$ kpc and the direction of the X-axis points from the Sun towards the Galactic center. Plots of the derived orbit projected onto the Galactic XY and XZ planes are shown as solid (blue) lines in Figure 11. In these projections, it is clear that the observed Virgo structure has just passed perigalacticon in its orbit after swooping in toward the Galactic center from a distance of > 50 kpc on a rather radial orbit. To give a sense of possible orbital paths of debris due to both the uncertainties in our orbital

⁶From the compilation of Dellomo & Newberg (2009), available at <http://homepages.rpi.edu/~newbeh/mwstructure/MilkyWayS>

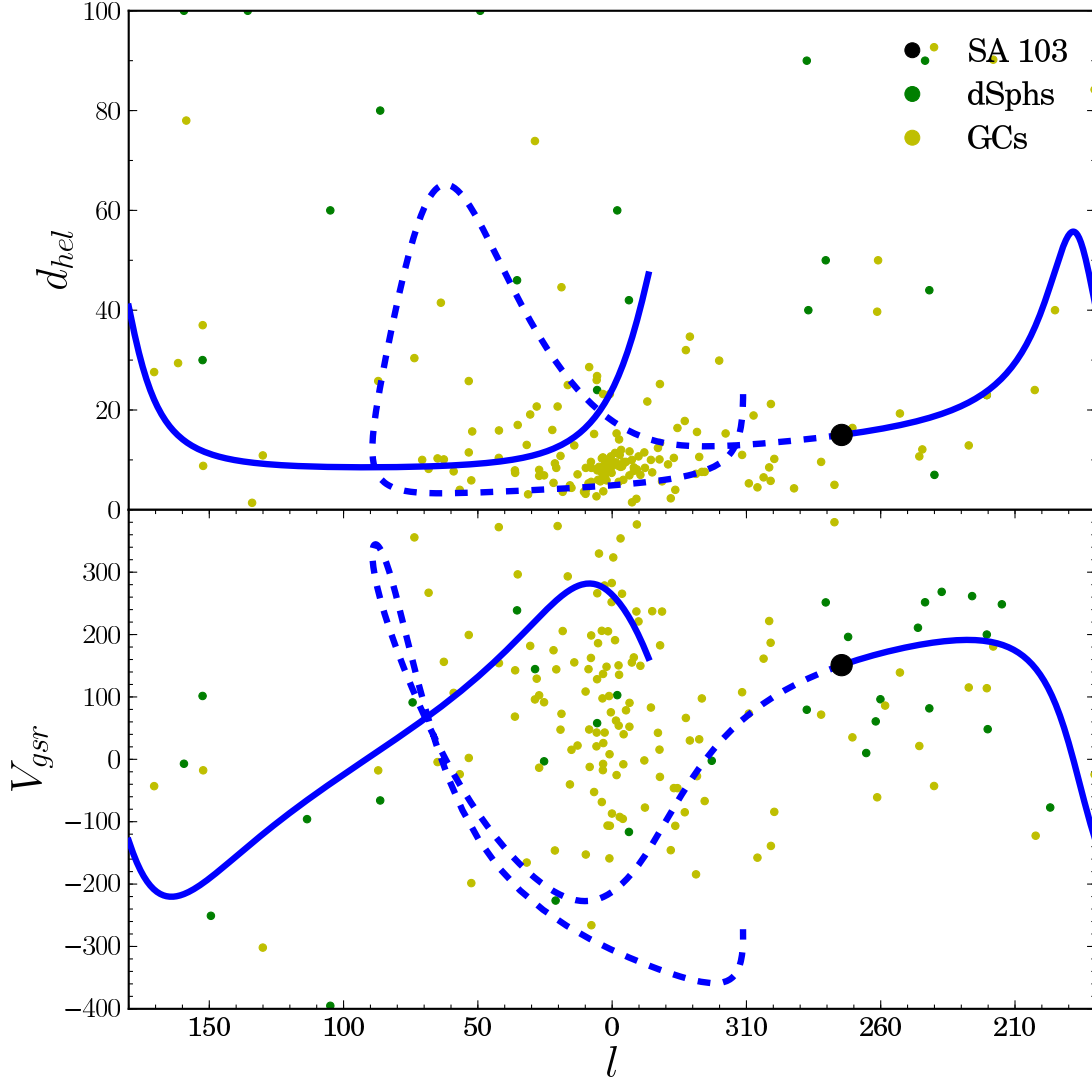


Fig. 10.— Derived orbit as a function of distance and V_{GSR} . The upper panel shows heliocentric distance vs. Galactic longitude for the derived Virgo substructure orbit (thick blue line). In the lower panel, we give V_{GSR} vs. Galactic longitude. Plots are labeled similarly as in Figure 9, with Galactic satellites (dSphs and GCs) shown as green/yellow dots. It is evident that the current Virgo debris is near orbital perigalacticon and has just passed fairly near the Galactic center.

parameters and the dispersion of 3-D velocities in the VOD, we show 10 orbits generated by randomly picking from within 1σ Gaussian distributions of the uncertainties on each of the orbital parameters in

Table 2. Most of these “perturbed” orbits do not depart drastically from the mean orbit.

These plots are similar in appearance to the orbits shown in CD09. Our orbit, derived from 16 stars rather than a single RR Lyrae, has similar eccentricity and apogalacticon as in the previous work, confirming that we have measured kinematics of debris from the same structure as the CD09 study. Note also that on first glance our data support (within the uncertainties) an association of NGC 2419 with the Virgo structure, as was suggested by CD09. This and other plausible orbital associations will be explored in the following section.

4.2. Possible Orbital Associations

To search quantitatively for possible orbital associations of satellites to our derived orbit, we compared the locations and velocities of known GCs and dSphs with the path and velocity of the mean orbit. This was done by defining a chi-squared value made up of the sum of the residuals (scaled by the uncertainties) in position and velocity between each point of the orbit and each Milky Way satellite’s known Galactic XYZ position and V_{GSR} velocity. The uncertainties in spatial positions at each orbital time-step were taken to be 30%, and in V_{GSR} to be 30 km s^{-1} . These large ranges should encompass the uncertainties in the kinematics used to generate the mean orbit.⁷ The minimum χ^2 is located for each object, with the assumption being that this represents the nearest point in phase space to the satellite. Globular clusters within 15 kpc of the Galactic center were excluded from the analysis because the Virgo substructure’s orbit will pass relatively near all of the globular clusters that are located within this region. Without 3-D kinematics for all of these inner GCs, it is difficult to assess their possible kinematical association with the Virgo orbit.

The globular cluster NGC 2419, which was claimed by CD09 to be plausibly associated with the Virgo orbit, is located ~ 30 kpc from the apocenter of our orbit. Note, however, that a slightly larger space velocity for Virgo debris at the SA 103 position would send an orbit through almost exactly the position of NGC 2419 (see, e.g., the maroon-colored “perturbed” orbit in Figure 11). The association of Virgo debris with this globular cluster is thus tentatively confirmed by our data.

The lowest χ^2 from our search (and, in fact, the only match with $\chi^2 < 5.0$) was for “SEGUE 1b”, which denotes the apparent velocity substructure found by Geha et al. (2009) and Simon et al. (2011) in the field of view of the ultra-faint dSph SEGUE 1. SEGUE 1 itself is spatially a good match to our Virgo substructure orbit, but the radial velocity predicted by our orbit agrees much better with the debris at $\sim 100 \text{ km s}^{-1}$ higher velocities (and roughly the same distance, according to Simon et al. 2011) than with SEGUE 1 itself.

In this section, we briefly discuss possible satellite associations found by our fitting technique as well as other known stellar overdensities; we will revisit each of these particular cases one-by-one in the following

⁷The assumption of a constant fractional uncertainty in the distance and fixed velocity uncertainty at all positions is chosen to simplify these calculations. In fact, for a given set of initial conditions and their associated uncertainties, the position and velocity uncertainties vary substantially at different points along the path of the orbit. Simulating this accurately would require a more sophisticated approach that is beyond the goals of this simple search for possible orbital associations.

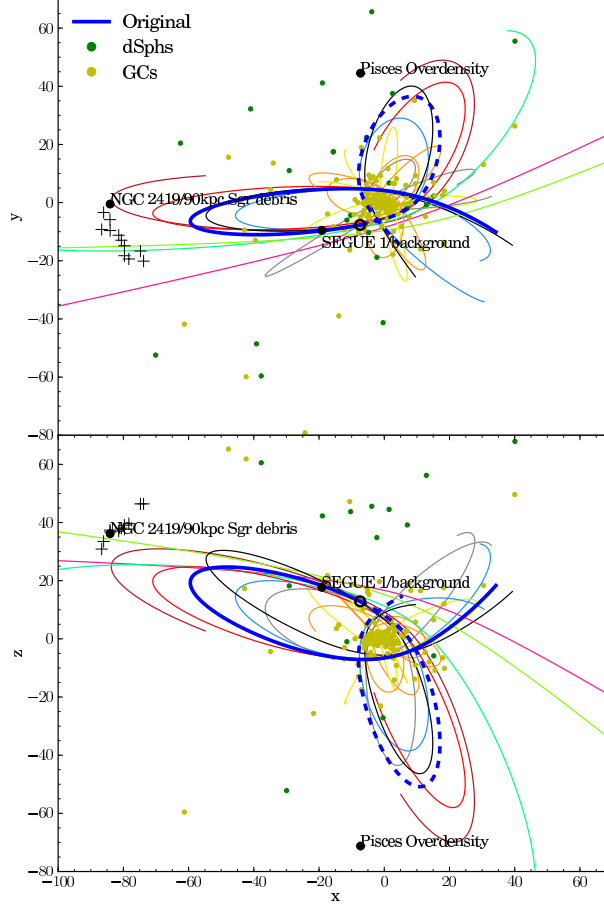


Fig. 11.— The upper panel shows the projection of the Virgo structure orbit onto the Galactic XY plane, and the lower panel gives the XZ projection. Thick blue lines are the orbit derived from our mean kinematics; solid blue lines are the forward integration, and dashed blue lines the backward integration. The thinner lines of other colors represent orbits generated by selecting from a Gaussian $1-\sigma$ distribution of the errors in the three velocity components and the distance, and illustrate the constraints placed on the Virgo progenitor orbit by our measurements. The Sun is at $(X, Y, Z) = (-8, 0, 0)$ kpc in this coordinate system, with positive X pointing in the direction from the Sun to the Galactic center. The position of SA 103 is represented as a large black circle. We also highlight as a large black dot the globular cluster NGC 2419, which was tentatively associated with the VSS by CD09, along with the “90 kpc Sgr debris” from Newberg et al. (2003) as plus signs. Two other substructures found to lie near our derived orbit – SEGUE 1 (or, more specifically, debris in the field of view of this ultra-faint dSph) and the Pisces Overdensity – are also given as large black dots.

section after we present the N -body model based on our orbit. The two main structures that were found to be consistent with the integrated orbit were NGC 2419 and the velocity substructure in the field of SEGUE 1 (which we denote “SEGUE 1b”). Another structure that may be related to the Virgo structure that is neither a GC nor a dSph is the Pisces Overdensity. This stellar overdensity is apparently located near a turnaround point in its orbit, and possibly contains distinct moving groups at positive and negative radial velocity, which further suggests that it is debris near apocenter of its orbit. An additional possibly-related structure is the debris previously claimed (Newberg et al. 2003) to be part of Sagittarius located at 90 kpc from the Galactic center, in close proximity to NGC 2419. These structures are briefly introduced here, and will be discussed in more detail in the following section of this work.

4.2.1. NGC 2419 / 90 kpc Sagittarius debris

NGC 2419 is located at $(l, b) = (180^\circ, 25^\circ)$ with heliocentric and Galactocentric distances of 84 and 91 kpc respectively. Its heliocentric radial velocity is -20 km s^{-1} , corresponding to a Galactic standard of rest velocity of -14 km s^{-1} (Peterson et al. 1986). Newberg et al. (2003) find an excess of A-type stars extending at least 10 degrees around NGC 2419 at about the same quoted distance. The authors claim that since NGC 2419 is contained within the debris, the tidal debris can be inferred to be at apogalacticon of its orbit, consistent with their findings of being coincident with a portion of the Sgr stream near its apogalacticon. However, this was merely a tentative association of these stars with Sagittarius; our current understanding of the Sgr tidal debris system (e.g., Law & Majewski 2010) suggests that there should not be debris at 90 kpc.

4.2.2. SEGUE 1

First discovered by Belokurov et al. (2007) using SDSS imaging data, this dwarf galaxy has subsequently been the subject of close examination because of its peculiar properties, most notably its apparent high mass-to-light ratio. Located at $(\text{RA}, \text{Dec}) = (152^\circ, 16^\circ)$ and $(l, b) = (220.5^\circ, 50.4^\circ)$ at a distance of $d_{\text{hel}} = 23 \pm 2 \text{ kpc}$ and $d_{\text{GC}} = 28 \text{ kpc}$, it is a good match to our derived orbit of the Virgo substructure. Belokurov et al. describe an apparent tidal tail feature extending from the northeast to the southwest in equatorial coordinates. However, subsequent studies have not been able to reproduce such results. A study by Geha et al. (2009) using Keck/DEIMOS spectroscopy presented radial velocity and metallicity data, and found a main grouping of stars at about $V_{\text{GSR}} = 111 \pm 1.3 \text{ km s}^{-1}$ with a smaller group of 4 stars at $\sim 200 \text{ km s}^{-1}$. They also obtain $[\text{Fe}/\text{H}] = -3.3 \pm 0.2$ for one of the SEGUE 1 stars. Simon et al. (2011) extended upon this survey using more data and obtain similar numbers to those of Geha et al. They also confirm the $\sim 200 \text{ km s}^{-1}$ feature from Geha et al. (2009), identifying 24 stars within the peak at $\langle V_{\text{GSR}} \rangle = 203.8 \pm 1.7 \text{ km s}^{-1}$, compared to the original 4 stars. These 24 stars represent a kinematically cold population, with $\sigma_V = 7.0 \pm 1.4 \text{ km s}^{-1}$. Simon et al. (2011) suggest that the stars making up this feature must be more metal-rich than those of SEGUE 1.

Our initial search for positional and kinematical associations to our Virgo orbit found SEGUE 1 was a fairly good match. However, we noticed that the $\sim 200 \text{ km s}^{-1}$ feature actually fits in better with our findings at the given location. Thus the chi-square test was rerun with an additional element, labeled “SEGUE 1b”, to distinguish it from the main SEGUE 1 population. The SEGUE 1b stars are an excellent match to our orbit in all three spatial dimensions (within 1.3 kpc), and offset from the best matching point by only $\sim 10 \text{ km s}^{-1}$ in radial velocity.

4.2.3. *The Pisces Overdensity*

The Pisces Overdensity was first found by Sesar et al. (2007) as an overdensity (dubbed “Structure J”) of distant RR Lyrae stars in SDSS Stripe 82. It was subsequently examined by Watkins et al. (2009) and shown to stretch across an area from $63^\circ < l < 93^\circ$ and $-60^\circ < b < -46^\circ$ at a Galactocentric distance of $79.4 \pm 14.1 \text{ kpc}$ and a metallicity of $[\text{Fe}/\text{H}] = -1.48 \pm 0.28$. Kollmeier et al. (2009) measured the radial velocities of RR Lyraes within SDSS Stripe 82 and found two distinct groups of stars, one centered at a heliocentric radial velocity of -75 km s^{-1} and the other around $-198 < V_r < -155 \text{ km s}^{-1}$. They find similar distances and metallicities as Watkins et al. Later, Sesar et al. (2010b) expanded the selection of stars of Kollmeier et al. and confirmed two distinct moving groups of Galactocentric velocity of $-52 \pm 11 \text{ km s}^{-1}$ and $50 \pm 3 \text{ km s}^{-1}$. This finding of two separate velocity groups in opposite directions suggests that this overdensity is at a turning point in its orbit. This too agrees nicely with the orbit that we have obtained in this area. Sharma et al. (2010) find a structure among 2MASS-selected M giants in the vicinity of the quoted location of the Pisces Overdensity, which is labeled “A16” in their paper. They find that the peak density lies just outside the range of SDSS Stripe 82. They hypothesize that the Pisces structure is an extended remnant of a satellite that was on a highly eccentric orbit and got tidally disrupted. However, in the same paper, they were not able to detect VSS members, calling into question such an association with VSS.

5. Discussion: the Progenitor of the Virgo Stellar Substructure

5.1. N-body Simulation

With the orbital parameters of Virgo debris well-constrained, we turn to the question of what type of progenitor could produce a structure with properties like those of the Virgo substructure. With the extant spatial and kinematical data, it is unclear whether all of the numerous detections of substructure in Virgo are related. However, we will show that a simple model based on our precise kinematics explains nearly all of the observed properties.

To understand the orbital dynamics of the Virgo substructure progenitor more clearly, semi-analytical N -body simulations were generated using our derived orbit. The kinematical parameters determined for Virgo debris in SA 103 were used to generate orbital models using the same gravitational potential as the test particle orbit. The simulation templates used were 10,000 particle Plummer spheres placed on our

derived orbit for the Virgo structure. The satellites were evolved in the Galactic potential for 3–4 Gyr using the `gyrfalcON` tool of the NEMO Stellar Dynamics Toolbox (Dehnen 2002), and their ending time tailored to place the core of the progenitor near the current VOD. This strategy of placing the progenitor (or its remains) at the position of the VOD is motivated by our derived orbit. Pile-ups of tidal debris are typically located at the apo- or peri-center of a satellite’s orbit; however, we showed in the previous section that our measured kinematics place Virgo substructure stars at an orbital phase just past pericenter. Thus, in order to have a cloud-like pile-up of stars at the VOD position (i.e., at an orbital phase that is *not* at peri- or apo-center), the stellar overdensity is likely the remains of the progenitor itself.

Because the progenitor of the Virgo structure is unknown (if it even still exists), we must explore the behavior of disrupting satellites of different masses. Initially, we placed a globular-cluster-sized object with $M = 1 \times 10^5 M_\odot$ and Plummer radius $r_{\text{pl}} = 50$ pc on our derived orbit. On the eccentric orbit derived for Virgo stars, the globular cluster is rapidly shredded upon its pericentric passage. The N -body results of this globular cluster progenitor are seen in Figure 12, which focuses on the region of sky around SA 103. The satellite is already extended into a narrow tidal stream after its first perigalactic passage (in the upper panel), and is completely disrupted by around 3 to 4 Gyr, corresponding to the third perigalactic passage. This creates a narrow, well defined stream in the sky, contrary to observations of a large cloud-like feature seen in Virgo. We note also that remnants of disrupted globular clusters are typically rather kinematically cold; the absence of a narrow velocity peak among the Virgo substructure data thus also argues against a globular cluster progenitor. Therefore, a globular cluster-like object is unlikely to be the progenitor of the substructure(s) in Virgo.

Having ruled out a globular cluster as the Virgo substructure progenitor, we then tried a larger, more massive dwarf galaxy-like satellite. Specifically, we first simulated a dSph of mass similar to that derived by Newberg et al. (2010) for the Orphan stream progenitor ($M = 3 \times 10^6 M_\odot$), configured in a Plummer sphere of radius $r_{\text{pl}} = 0.2$ kpc. This low-mass dwarf galaxy was run through an N -body simulation with the same MW parameters as the globular cluster model, on our derived Virgo substructure orbit. As with the globular cluster, the Orphan-like progenitor disrupts quickly on this destructive orbit. As can be seen in Figure 13, this comparatively kinematically “warmer” object dissolves much more rapidly than the globular cluster. The remnant becomes more “puffy” than the disrupted globular cluster, but still remains embedded in a narrow stream. This more closely resembles what is seen in Virgo, and suggests that an even larger, more massive dSph may produce a large-area, cloud-like overdensity when disrupted on this orbit.

Finally, we simulated a 10,000 particle, Sagittarius-sized template dwarf galaxy (a Plummer sphere with mass of $M \sim 10^9 M_\odot$ and scale radius $r_{\text{pl}} = 0.9$ kpc) on the Virgo test-particle orbit. The results of this gravitational N -body simulation are displayed in Figures 14 (spatial distribution), 15 (V_{GSR} and distance vs. longitude), and 16 (polar projection of the spatial positions). The disruption of a Sgr-sized object on this orbit produces several structures that span large (hundreds of square degree) areas of the sky (Figure 14). The large, diffuse overdensities centered at $(l, b) \sim (60^\circ, -50^\circ)[(\alpha, \delta) \sim (330^\circ, -5^\circ)]$ and $(l, b) \sim (210^\circ, 40^\circ)[(\alpha, \delta) \sim (110^\circ, 20^\circ)]$ are the results of tidal debris piling up at apogalacticon. These distant debris (at $R_{\text{GC}} \sim 80$ and ~ 50 kpc, respectively; see Figure 15) piling up at the turning points of the disrupting dSph’s orbit are expected for an object on such a radial, destructive orbit (see, e.g., the “umbrella-

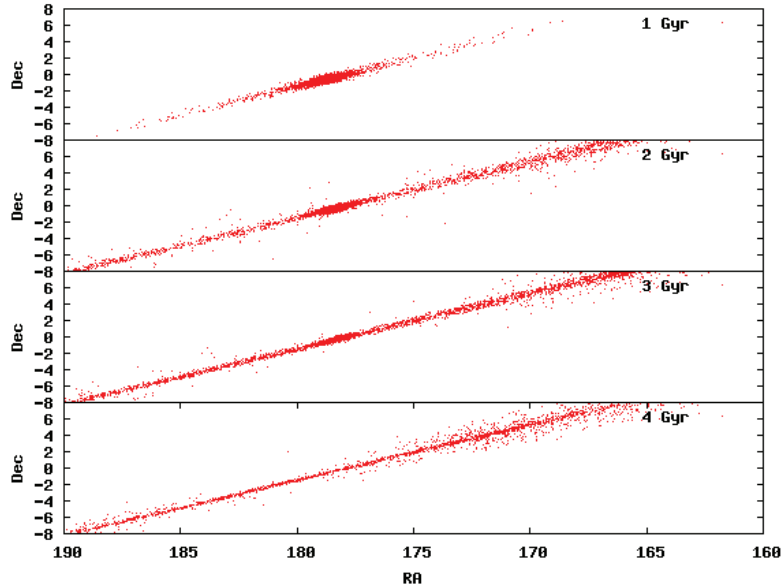


Fig. 12.— Shown here is an N -body simulation of a globular cluster sized object evolved along the derived test particle orbit, in 4 different time slices, spaced 1 Gyr apart. The cluster is modeled as a Plummer sphere with mass of $M = 1 \times 10^5 M_\odot$ and Plummer scale radius of 50 pc, represented by 10,000 red particles of equal mass. The object is seen to rapidly stretch out into a thin filament, falling apart between 3-4 Gyr, or after 3 perigalactic passages.

like” structures in Johnston et al. 2008). One may expect a dSph seen shortly after a perigalactic passage to have a distorted morphology with well-defined tidal tails emanating from it. However, the N -body model guided by our precise kinematics of Virgo stars shows that the large tidal shock imparted to a Sgr-like progenitor upon its passage < 10 kpc from the Galactic center causes the dSph to inflate to an apparent size (at $d = 15$ kpc) of hundreds of square degrees (note that we are not concerning ourselves about whether the particles are bound to the progenitor at this stage; most of the stars must be unbound at this point in the object’s evolution). This is seen more clearly in the left panel of Figure 16, which shows a polar plot of N -body model debris in Galactic coordinates, centered on the north Galactic pole. Given for comparison in the right panel of Figure 16 is a reproduction of Figure 5 from Newberg et al. (2007), in which the Virgo substructure is clearly seen as an overdensity of photometrically-selected F-turnoff stars from SDSS. The progenitor (or its remains) in our model spans roughly the same area as the overdensity seen by Newberg et al., centered on the same position, including possibly an elongated shape along Galactic latitude (i.e., from left to right in the figure).

This structure, seen at roughly the position of SA 103 (denoted by the large black dot in Figure 14 at $(l, b) \sim (275^\circ, 59^\circ)$, or $(\alpha, \delta) \sim (179^\circ, -1^\circ)$) and spanning ~ 500 square degrees, contains $\sim 16\%$ of the original 10,000 particles making up the progenitor. Since the progenitor had a mass of $10^9 M_\odot$, this

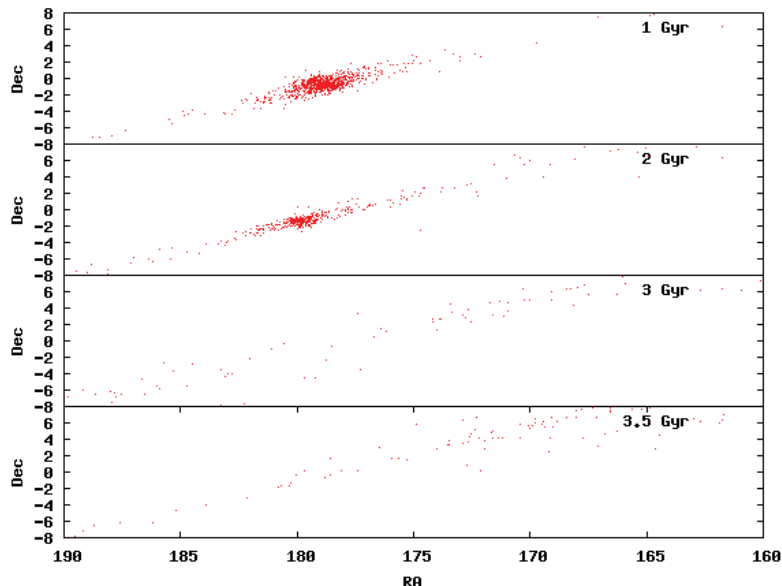


Fig. 13.— Results of an N -body simulation of an Orphan-like progenitor (a dwarf-galaxy-sized object) evolved along our derived Virgo structure orbit. The panels show snapshots at the position of SA 103 in four time slices spaced ~ 1 Gyr apart. This object was configured as a Plummer sphere with mass of $M = 3 \times 10^6 M_\odot$ and a scale radius of 200 pc. The satellite dissolves quickly (in less than 3 Gyr), with the remnant showing a narrow stream-like structure at early times and virtually no spatial concentration at later stages.

corresponds to a mass of $\sim 1.6 \times 10^8 M_\odot$ in the area surrounding the remains of the progenitor. As an exercise, we estimate the luminosity corresponding to this mass by assuming a mass-to-light ratio typical of Milky Way dSphs,⁸ $(\frac{M}{L})_\odot = 100$ (see, e.g., Wolf et al. 2010, Walker et al. 2009, Simon & Geha 2007); this yields a V -band absolute magnitude of $M_V = -10.7$ (or $M_V = -13.2, -8.2$, respectively, for $\frac{M}{L}_\odot = 10, 1000$). This compares favorably to the estimate of the total integrated light of the VOD by Prior et al. (2009) in a 760 deg^2 area of $M_V = -11.9$ (or $M_V = -10.1$ using the more nearby Jurić et al. 2008 distances). Jurić et al. (2008) found a total r -band luminosity of $0.1 \times 10^6 L_\odot$, or $M_r = -7.8$, for the overdensity assuming a distance of 10 kpc and 1000 deg^2 area. Thus, the remains of the Virgo progenitor as determined by our derived orbit are consistent with the observed stellar overdensity that covers hundreds of square degrees.

Another mystery surrounding the numerous overdensities detected in Virgo is the disagreement among radial velocities between studies of debris at different positions. As we showed in Section 3, even in SA 103, which spans only $40' \times 40'$, there is a significant excess of high- V_{GSR} stars that forms a broad peak (see

⁸In our model, the object is probably no longer a bound system, making the assumptions of these calculations dubious. We present these results simply as an attempt to compare N -body particles to the observed stellar overdensity.

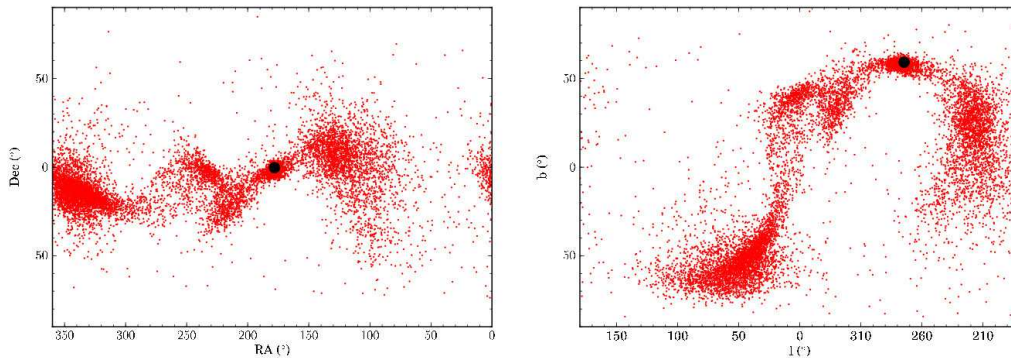


Fig. 14.— The results of an N -body simulation of a Sagittarius-sized ($M = 1 \times 10^9 M_{\odot}$, $r_{\text{pl}} = 0.9$ kpc) Plummer sphere on our derived Virgo substructure orbit. The left panel depicts the debris in equatorial coordinates and the right panel shows the simulation results in Galactic coordinates. The black point represents the present location of the observed Virgo debris in SA 103. This N -body simulation was initially placed 3 Gyr in the past and integrated forwards for 2.95 Gyr. Three overdensities are immediately apparent: The ones at $l = 60^{\circ}$ and $l = 210^{\circ}$ are due to piling up of debris at apogalacticon. The third overdensity located at $l = 270^{\circ}$ is progenitor related; in other words, the location of this cloud of debris changes depending on the duration of the simulation. We tailored the run-time of this particular simulation to place the progenitor (or its remains) at this position.

Figure 3). This is more obvious among SDSS RVs shown in Figure 4 – a broad excess relative to the Besançon model is apparent at $100 \lesssim V_{\text{GSR}} \lesssim 250 \text{ km s}^{-1}$. This is much too broad to be the signature of a kinematically-cold tidal stream. If the VOD were due to the piling up of tidal debris at the apocenter of a satellite orbit, then a large velocity dispersion could be expected; however, the mean velocity at such a turnaround point must be $V_{\text{GSR}} \sim 0 \text{ km s}^{-1}$ rather than $\sim 150 \text{ km s}^{-1}$ as observed. Furthermore, we have shown that stars in the Virgo substructure are not at apogalacticon, having rather just passed their *peri*-galacticon. Examination of the upper panel of Figure 15, however, shows that our N -body model offers an explanation for the large spread in velocity of Virgo debris. The progenitor, having just experienced a close encounter with the Galactic center, has been kinematically heated so that its velocity dispersion has increased to $\sim 20 \text{ km s}^{-1}$ or more and its RVs span $\sim 100 \text{ km s}^{-1}$. Note that the model seen in Figure 15 does not predict debris with $V_{\text{GSR}} > 200 \text{ km s}^{-1}$ near the progenitor, as is seen in both the SA 103 data (Figure 3) and SDSS (Figure 4) as a long tail to high velocities. It is possible that additional substructure is present in this region of the sky. Alternatively, this long tail may be a feature of the disrupting Virgo progenitor that our simple model has not addressed – further modeling exploring the progenitor’s mass and mass distribution may be able to reproduce this feature.

To summarize, our N -body model of a Sagittarius-sized dwarf galaxy with mean kinematics of the 16 stars we determined to be Virgo substructure members qualitatively reproduces many of the observed properties of the stellar excess in Virgo. We have shown that a large, cloud-like stellar structure like that in Virgo is likely to have originated in the tidal disruption of a massive dwarf galaxy. No dwarf galaxies are found

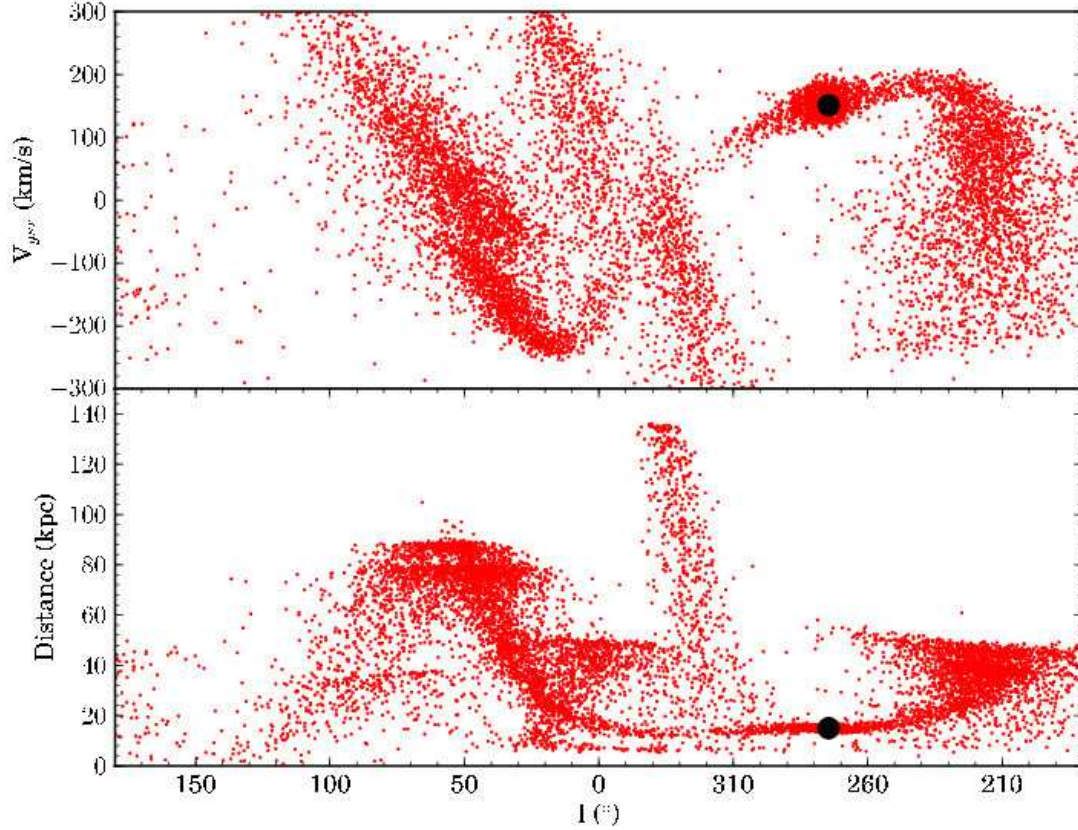


Fig. 15.— N -body results from the simulation with a Sagittarius-like progenitor, as in Figure 14. The upper panel shows V_{GSR} vs Galactic longitude while the lower panel shows heliocentric distance vs. Galactic longitude. The model runtime was tailored to place the progenitor (and/or its remains) at the position of SA 103 (the large black dot).

along the integrated path of the orbit we have derived, leading us to conclude that the Virgo substructure is itself the remains of the progenitor. The slight mismatch in the position of the disrupted progenitor in our model and that of the observed overdensity in Virgo is a consequence of the model runtime and our lack of knowledge of the central position of the stellar overdensity, which may lie outside the observed SDSS footprint. Details such as the size of the overdensity and the direction of its elongation may also be slightly discrepant between the model and observations, but are in rough qualitative agreement. Many of these differences are likely due to the fact that the initial conditions used to generate the model – namely, the kinematics of debris in SA 103 – may not actually correspond to the center of the progenitor. A more comprehensive exploration of parameter space (including, but not limited to, the mass of the progenitor, its position, and its initial density configuration) could likely resolve some of these issues, but is beyond the

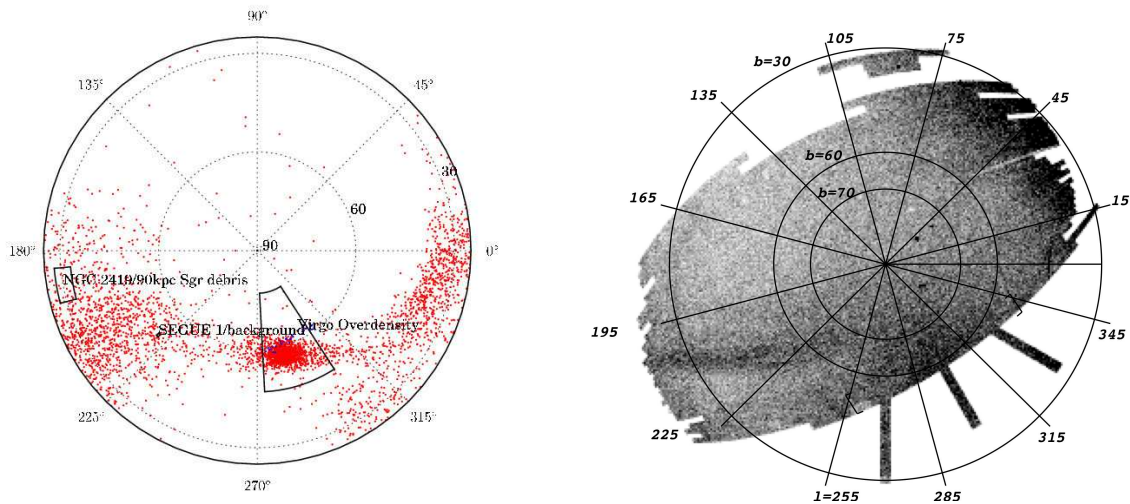


Fig. 16.— Left panel: the Sagittarius-sized N -body simulation in polar Galactic coordinates, centered at the North Galactic Cap. Here an overdense region around $(l, b) = (285^\circ, 55^\circ)$ is clearly visible. Approximate boundaries of the possible associations are also drawn in the plot. Right panel: Density map of F-turnoff stars in the Northern Galactic Cap from Newberg et al. 2007. These stars were obtained from SDSS DR5 based on the criteria $0.2 < (g-r)_0 < 0.3$, $(u-g)_0 > 0.4$, and $20.0 < g_0 < 21.0$. Darker areas contain more F turnoff stars. Comparing this figure to the left panel, one can see an apparent agreement between the observed location of the Virgo debris and that predicted by the N -body model. The Virgo overdensity is visible at the lower right edge of the data in the right panel.

scope of this work. It is clear, however, that the morphology, spatial extent, luminosity, and large velocity dispersion of the observations are all qualitatively consistent with our simple model. We thus suggest that a massive dwarf galaxy was the progenitor of the substructure in Virgo.

5.2. Other Possible Progenitors or Associated Overdensities

In Section 4.1 we discussed a search for Milky Way satellites and stellar overdensities that may be associated with the Virgo substructure. While initially the search was conducted in hopes of identifying the progenitor of the VOD, our modeling results suggest that the VOD itself is likely the remains of the progenitor. However, the infalling dwarf spheroidal that produced the VOD may have had satellites of its own, similar to the globular clusters associated with the Sgr and Fornax dSphs. If the progenitor had globular clusters orbiting in its potential, these should be found along the orbit of the progenitor. Also, since the VOD is near the pericenter of the progenitor’s rather destructive orbit, there should be additional tidal debris that has collected at the apogalactica of the orbit, as seen in Figures 14 and 15. In this subsection, we revisit the satellites and stellar substructures we identified in Section 4.2, and discuss them in the context of the N -body model results.

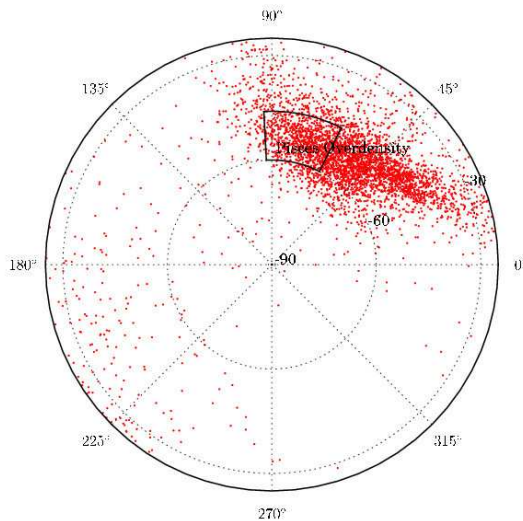


Fig. 17.— N -body model debris in the southern Galactic hemisphere. An overdensity of model debris is seen that is nearly coincident with the Pisces Overdensity between $60 \lesssim l \lesssim 90^\circ$. These stars, located at distances of ~ 80 – 90 kpc, correspond to the apogalacticon of our derived orbit.

5.2.1. NGC 2419 and Nearby 90-kpc Stellar Overdensity

The distant Milky Way globular cluster NGC 2419 was suggested by CD09 to be plausibly associated with their orbit of the VSS based on a single RR Lyrae star. The orbit passes near NGC 2419 at the next apocenter ahead of the Virgo substructure along its orbit. The cluster has a radial velocity of $\langle V_{\text{GSR}} \rangle = -14$ km s $^{-1}$, which, because it is close to zero, is consistent with NGC 2419 being at the turnaround point of its orbit. We find that our orbit does not reach the ~ 80 kpc distance of NGC 2419, instead turning around at ~ 50 kpc at its nearest apocenter. However, within the uncertainties on the orbital parameters (as illustrated by the different orbits in Figure 11 with kinematics selected from within the $1 - \sigma$ uncertainties), the orbit could plausibly be associated with a satellite or debris at such distances. NGC 2419 is an unusually large, luminous globular cluster, which has led to speculation that it is actually the stripped core of a former dwarf spheroidal galaxy (e.g., van den Bergh & Mackey 2004; Mackey & van den Bergh 2005; Cohen et al. 2010, 2011). One might thus suggest NGC 2419 to be the progenitor of the Virgo substructure. We believe this is unlikely, because NGC 2419 has a metallicity of $[\text{Fe}/\text{H}] = -2.1$ (Suntzeff et al. 1988), making it more metal-poor than the debris we have studied in SA 103, and even more deficient than the RR Lyrae studies have found for VOD/VSS stars. Because metallicity gradients in dwarf galaxies lead to more metal-rich populations being concentrated at their cores, tidal streams from disrupted dSphs should have mean metallicities that decrease with distance along the stream from the progenitor (e.g. Chou et al. 2007). It is hard to imagine how, if NGC 2419 is the progenitor, it could have a mean metallicity lower than that of all known debris. It is also possible that the cluster fell in with the (dwarf-galaxy) progenitor. However, we note that van den Bergh (2007) pointed out that the globular clusters associated with dwarf galaxies are

faint relative to the general globular cluster population; this would appear to rule out the extremely luminous NGC 2419 as a globular-cluster companion of an infalling dwarf galaxy.

Furthermore, Newberg et al. (2003) identified an overdensity of A-type (primarily BHB) stars at a mean distance of 83 kpc spanning over 200 deg^2 in the region surrounding NGC 2419. Very few BHB stars should be present that far out in the halo, and it was originally suggested by Newberg et al. that these stars are Sagittarius tidal debris. In our N -body model of the Virgo progenitor, the position of the Newberg et al. (2003) stars on the sky is consistent with the collection of Virgo-structure stars at the apocenter of its orbit. We note that the N -body model produces debris about 40% closer than either NGC 2419 or the Newberg et al. stars, but this is not troubling. The orbit traverses distances consistent with both NGC 2419 and the A-star overdensity, and we have seen that N -body models using slightly different kinematics (from within our error distribution) would produce model debris at those distances as well. We thus suggest that NGC 2419 and the “cloud” of A stars nearby it may be associated with the Virgo progenitor.

5.2.2. Substructure in SEGUE 1 Field of View

Another of the close matches to our orbit is the dwarf galaxy SEGUE 1, which lies directly along the path of the Virgo structure orbit. However, we are not suggesting here that the extremely metal-poor, dark matter-dominated SEGUE 1 dSph is associated with the Virgo structure. Instead, it is the “extra” radial velocity peak identified by Geha et al. (2009, with 4 stars), later seen more strongly by Norris et al. (2010, 8 stars), and finally detected with 24 stars by Simon et al. (2011) that we believe to be tidal debris from the Virgo system. Because the spectroscopic targets were selected by Simon et al. to be consistent with the SEGUE 1 distance ($23 \pm 2 \text{ kpc}$), the stars in the additional RV peak are presumably at roughly this same distance (Simon et al. 2011 quote a distance of $\approx 22 \text{ kpc}$). However, their mean velocity is at $V_{\text{GSR}} = 204 \text{ km s}^{-1}$, offset by $\sim 100 \text{ km s}^{-1}$ from the SEGUE 1 velocity. Our N -body model predicts Virgo debris should be present at this position ($l, b = 220, 50^\circ$) at a distance of $\sim 25 \text{ kpc}$ (see Figures 14 and 15). Furthermore, the upper panel of Figure 15 shows that the debris in our model is at $150 < V_{\text{GSR}} < 200 \text{ km s}^{-1}$, or almost exactly where the 24 “excess” stars in the Simon et al. (2011) study appear. We therefore conclude that the debris in the SEGUE 1 field of view is plausibly associated with the Virgo stream system. We note also that the mean metallicity is suggested by Simon et al. (2011) to be $[\text{Fe}/\text{H}] = -1.3$ for these 24 stars in the “ 300 km s^{-1} stream”. This is consistent with the metallicity we have measured for debris in SA 103. Lending further credence to our claim of an association with the stream from the Virgo progenitor is the fact that both Simon et al. (2011) and Niederste-Ostholt et al. (2009) see an east-west extension of the 300 km s^{-1} stream stars. In fact, Figure 8b of Simon et al. (2011) shows the stars in this velocity feature to possibly be oriented along a southeast-to-northwest direction, which is exactly the orientation of the debris from our model of the Virgo progenitor. Based on all these facts taken together, we believe that the 300 km s^{-1} stream in the SEGUE 1 field of view is debris associated with the Virgo substructure.

5.2.3. *Pisces Overdensity*

Finally, we note that the “Pisces Overdensity”, a stellar excess spanning a large area on the sky at a Galactocentric distance of 79 ± 14 kpc (Sesar et al. 2007; Watkins et al. 2009), is located at the position and distance of the most recent apocenter of our Virgo orbit. This overdensity was first found among RR Lyrae in SDSS Stripe 82 data at $(\alpha, \delta) \sim (355^\circ, 0^\circ)$, or $(l, b) \sim (88^\circ, -58^\circ)$, and subsequently seen to stretch to $(l, b) \sim (105^\circ, -53^\circ)$ in 2MASS-selected M-giant stars (Sharma et al. 2010). Examination of Figures 14 and 15 shows a pile-up of model debris at the position and near the distance roughly corresponding to the Pisces Overdensity. This is also illustrated in the polar view of model debris in the southern Galactic cap seen in Figure 17, which overplots the approximate location of the Pisces Overdensity atop our model. Because this substructure has been detected in metal-poor RR Lyrae (Sesar et al. 2007; Watkins et al. 2009) as well as relatively metal-rich 2MASS-selected M-giant stars (Sharma et al. 2010), it has already been suggested to be related to a dwarf-galaxy disruption event. It is therefore remarkable that our N -body model for a disrupting dSph on the Virgo orbit predicts just such a “cloud” of tidal debris as has been observed. The radial velocity one would expect at the turnaround point of the orbit is $V_{\text{GSR}} = 0 \text{ km s}^{-1}$, with some large spread about zero velocity due to the viewing angle roughly along the path of both the outward-streaming and inward-bound debris (see Figure 15 for an illustration of the large range of expected V_{GSR} in a $\sim 20^\circ$ range of Galactic longitude). Spectroscopy of RR Lyrae in the Pisces structure by Kollmeier et al. (2009) was combined with additional spectra by Sesar et al. (2010a) to arrive at a sample of 12 RR Lyrae in the overdensity. These 12 stars separate into two distinct peaks at $\langle V_{\text{GSR}} \rangle = 50 \pm 3 \text{ km s}^{-1}$ with $\sigma = 10 \pm 3 \text{ km s}^{-1}$, and $\langle V_{\text{GSR}} \rangle = -52 \pm 11 \text{ km s}^{-1}$, $\sigma = 23 \pm 9 \text{ km s}^{-1}$. Sesar et al. (2010a) considered the possibility that the two groups are drawn from the same Gaussian distribution, and concluded that the hypothesis of normality can be rejected at the $\sim 95\%$ level. However, from the small number of stars, it is unclear whether the two RV peaks correspond to approaching and receding portions of the same tidal stream, or separate substructures. However, it is reasonable to conclude that either (or perhaps both) of these velocities are consistent with debris from the Virgo progenitor as modeled by us. We note, though, that Sesar et al. (2010a) find that although the two velocity groups are centered at roughly the same positions, one of the stars in the negative-velocity group extends to lower right ascension. Similarly, in Figures 12 and 14 of Watkins et al. (2009) the Pisces Overdensity appears to be closer at lower RA (and lower Galactic longitude) than at its peak. Both of these findings are consistent with our tidal stream model, wherein the debris on the lower-longitude side of the apoGalacticon is on the approaching portion of the stream. We conclude that it is likely that the Pisces Overdensity has its origin in the disruption of the Virgo progenitor. However, further observations and detailed modeling of both the Virgo and Pisces structures are needed to confirm this.

6. Conclusion

We have presented 3-D kinematics of candidate Virgo substructure members in SA 103, a $40' \times 40'$ field located at $(\alpha, \delta)_{2000} = (178.75^\circ, -0.59^\circ)$, or $(l, b) = (274.6^\circ, 59.1^\circ)$. This work builds upon that of CD09, in which an orbit was presented for a single VSS RR Lyrae candidate from the SA 103 data set. We have obtained follow-up spectra of a total of 215 stars from the Kapteyn’s Selected Areas proper motion

survey outlined in Casetti-Dinescu et al. (2006). From the derived radial velocities, we isolate an excess of relatively high-velocity stars that are unexpected from smooth Milky Way populations. These stars, at $100 \lesssim V_{\text{GSR}} \lesssim 350 \text{ km s}^{-1}$, do not make up a kinematically cold “peak” in the RVs, but rather span nearly the entire high-velocity range. However, we show that the proper motions of most of the stars from these high velocities are consistent with their being kinematically associated. Furthermore, these high-velocity stars inhabit regions of the color-magnitude diagram that place them all at nearly the same distance, $\sim 14 \pm 3$ kpc, from the Sun.

We identify a total of 16 candidate Virgo substructure members, from which we derive a weighted mean radial velocity $V_{\text{GSR}} = 152.6 \pm 22.0 \text{ km s}^{-1}$ and proper motion $(\mu_\alpha \cos \delta, \mu_\delta) = (-5.24, -0.91) \pm (0.43, 0.46) \text{ mas yr}^{-1}$. The mean metallicity of the substructure is estimated to be $[\text{Fe}/\text{H}] \sim -1.1$. From the mean kinematics and the derived distance of 14 ± 3 kpc, we generate an orbit in a model Galactic potential. The Virgo substructure stars are on an eccentric orbit ($e = 0.81^{+0.10}_{-0.27}$) with peri- and apo-centers of $R_p = 5.6^{+0.9}_{-0.8}$ kpc and $R_a = 52^{+87}_{-24}$ kpc, respectively.

We searched for satellites or known overdensities that can plausibly be associated with the Virgo progenitor. Based on the positions and radial velocities of the derived orbit, we find that known tidal debris in the field of view of the ultra-faint dwarf SEGUE I match our predicted orbit in position and velocity. While it is intriguing to find such a close match to the predicted path and kinematics of the Virgo progenitor orbit, one must explain the fact that the 24 stars making up the “ 300 km s^{-1} debris” near SEGUE I were found by Simon et al. (2011) to have a velocity dispersion of only 7.0 km s^{-1} . It is possible that these stars near SEGUE I, as well as many of the apparently cold stellar substructures in Virgo, are kinematically cold sub-clumps within the Virgo debris. Another plausible match to our derived orbit is the globular cluster NGC 2419. This distant cluster was suggested by CD09 to be associated with the Virgo substructure, possibly as its progenitor. It is difficult to explain how the metal-poor ($[\text{Fe}/\text{H}] = -2.1$) NGC 2419 could have been the origin of the more metal-rich Virgo debris; rather, it is more likely that NGC 2419 fell into the Milky Way with the Virgo progenitor. We also note that there is a known overdensity of A-stars found by Newberg et al. (2003) to span $\sim 200 \text{ deg}^2$ around NGC 2419 at a mean distance of 83 kpc. This cloud of stars may be associated with NGC 2419, the Virgo progenitor, or both.

Through the use of N -body models of satellites on this rather destructive orbit, we show that the large spatial extent of the Virgo substructure does not arise if the progenitor of the stellar overdensity was a globular cluster or low-mass dwarf galaxy. Rather, the progenitor of the Virgo structure must have been a massive, Sagittarius-like dwarf spheroidal galaxy of mass $\sim 10^9 M_\odot$. The N -body model of a Sgr-mass dSph on our derived orbit qualitatively reproduces the observed spatial extent, velocity spread, and estimated stellar mass of the Virgo overdensity. We thus conclude that the entire cloud-like Virgo substructure is likely the tidal debris remnant from a recently-disrupted dwarf galaxy. Our model also produces a “cloud” of debris near the position and distance of NGC 2419 (and the surrounding A-star overdensity), corresponding to the apocenter of the orbit. Another diffuse overdensity is predicted by the model near the location of the Pisces Overdensity, suggesting that the Pisces stars may have originated in the Virgo progenitor.

We appreciate useful discussions with Kathryn Johnston about the expected properties of “cloud-like”

debris structures, and thank the referee for thoughtful comments that improved the manuscript. J. L. C. and H. J. N. gratefully acknowledge the support of National Science Foundation grant AST 09-37523.

Facilities: WIYN (Hydra), Blanco (Hydra), Sloan, MtW:1.5m, Du Pont

Funding for the SDSS and SDSS-II has been provided by the Alfred P. Sloan Foundation, the Participating Institutions, the National Science Foundation, the U.S. Department of Energy, the National Aeronautics and Space Administration, the Japanese Monbukagakusho, the Max Planck Society, and the Higher Education Funding Council for England. The SDSS Web Site is <http://www.sdss.org/>.

The SDSS is managed by the Astrophysical Research Consortium for the Participating Institutions. The Participating Institutions are the American Museum of Natural History, Astrophysical Institute Potsdam, University of Basel, University of Cambridge, Case Western Reserve University, University of Chicago, Drexel University, Fermilab, the Institute for Advanced Study, the Japan Participation Group, Johns Hopkins University, the Joint Institute for Nuclear Astrophysics, the Kavli Institute for Particle Astrophysics and Cosmology, the Korean Scientist Group, the Chinese Academy of Sciences (LAMOST), Los Alamos National Laboratory, the Max-Planck-Institute for Astronomy (MPIA), the Max-Planck-Institute for Astrophysics (MPA), New Mexico State University, Ohio State University, University of Pittsburgh, University of Portsmouth, Princeton University, the United States Naval Observatory, and the University of Washington.

REFERENCES

- Abadi, M. G., Navarro, J. F., Steinmetz, M., & Eke, V. R. 2003, *ApJ*, 591, 499
- An, D., Johnson, J. A., Clem, J. L., et al. 2008, *ApJS*, 179, 326
- An, D., Johnson, J. A., Beers, T. C., et al. 2009, *ApJ*, 707, L64
- Belokurov, V., Zucker, D. B., Evans, N. W., et al. 2007, *ApJ*, 654, 897
- Brink, T. G., Mateo, M., & Martínez-Delgado, D. 2010, *AJ*, 140, 1337
- Bullock, J. S., & Johnston, K. V. 2005, *ApJ*, 635, 931
- Carlin, J. L., Majewski, S. R., Casetti-Dinescu, D. I., Law, D. R., Girard, T. M., & Patterson, R. J. 2012, *ApJ*, 744, 25
- Casetti-Dinescu, D. I., Girard, T. M., Majewski, S. R., Vivas, A. K., Wilhelm, R., Carlin, J. L., Beers, T. C., & van Altena, W. F. 2009, *ApJ*, 701, L29
- Casetti-Dinescu, D. I., Majewski, S. R., Girard, T. M., Carlin, J. L., van Altena, W. F., Patterson, R. J., & Law, D. R. 2006, *AJ*, 132, 2082
- Casey, A. R., Keller, S. C., & Da Costa, G. 2012, *AJ*, 143, 88

- Chonis, T. S., Martínez-Delgado, D., Gabany, R. J., Majewski, S. R., Hill, G. J., Gralak, R., & Trujillo, I. 2011, *AJ*, 142, 166
- Chou, M., Majewski, S. R., Cunha, K., et al. 2007, *ApJ*, 670, 346
- Cohen, J. G., Huang, W., & Kirby, E. N. 2011, *ApJ*, 740, 60
- Cohen, J. G., Kirby, E. N., Simon, J. D., & Geha, M. 2010, *ApJ*, 725, 288
- Dehnen, W. 2002, *Journal of Computational Physics*, 179, 27
- Dellomo, J., & Newberg, H. J. 2009, *Bulletin of the American Astronomical Society*, 41, #425.11
- Duffau, S., Vivas, A. K., Zinn, R., Méndez, R. A., & Ruiz, M. T. 2010, in *IAU Symposium*, Vol. 262, IAU Symposium, ed. G. Bruzual & S. Charlot, 131–134
- Duffau, S., Zinn, R., Vivas, A. K., Carraro, G., Méndez, R. A., Winnick, R., & Gallart, C. 2006, *ApJ*, 636, L97
- Font, A. S., Johnston, K. V., Bullock, J. S., & Robertson, B. E. 2006, *ApJ*, 646, 886
- Friel, E. D. 1987, *AJ*, 93, 1388
- Geha, M., Willman, B., Simon, J. D., Strigari, L. E., Kirby, E. N., Law, D. R., & Strader, J. 2009, *ApJ*, 692, 1464
- Girardi, L., Grebel, E. K., Odenkirchen, M., & Chiosi, C. 2004, *A&A*, 422, 205
- Grillmair, C. J. 2010, in *Galaxies and their Masks*, ed. D. L. Block, K. C. Freeman, & I. Puerari, 247
- Johnson, D. R. H., & Soderblom, D. R. 1987, *AJ*, 93, 864
- Johnston, K. V. 1998, *ApJ*, 495, 297
- Johnston, K. V., Bullock, J. S., Sharma, S., Font, A., Robertson, B. E., & Leitner, S. N. 2008, *ApJ*, 689, 936
- Jones, L. A. 1998, PhD thesis, The University of North Carolina at Chapel Hill
- Jurić, M., Ivezić, Ž, Brooks, A., et al. 2008, *ApJ*, 673, 864
- Kapteyn, J. C. 1906, Plan of selected areas (Groningen, Hoitsema brothers, 1906.)
- Keller, S. C. 2010, *PASA*, 27, 45
- Keller, S. C., da Costa, G. S., & Prior, S. L. 2009, *MNRAS*, 394, 1045
- Keller, S. C., Murphy, S., Prior, S., Da Costa, G., & Schmidt, B. 2008, *ApJ*, 678, 851
- Kollmeier, J. A., Gould, A., Sheckman, S., et al. 2009, *ApJ*, 705, L158

- Law, D. R., Johnston, K. V., & Majewski, S. R. 2005, *ApJ*, 619, 807
- Law, D. R., & Majewski, S. R. 2010, *ApJ*, 714, 229
- Mackey, A. D., & van den Bergh, S. 2005, *MNRAS*, 360, 631
- Majewski, S. R. 1993, *ARA&A*, 31, 575
- Majewski, S. R., Munn, J. A., & Hawley, S. L. 1996, *ApJ*, 459, L73+
- Majewski, S. R., Skrutskie, M. F., Weinberg, M. D., & Ostheimer, J. C. 2003, *ApJ*, 599, 1082
- Martínez-Delgado, D., Gómez-Flechoso, M. Á., Aparicio, A., & Carrera, R. 2004, *ApJ*, 601, 242
- Martínez-Delgado, D., Gabany, R. J., Crawford, K., et al. 2010, *AJ*, 140, 962
- Miyamoto, M., & Nagai, R. 1975, *PASJ*, 27, 533
- Muñoz, R. R., Carlin, J. L., Frinchaboy, P. M., Nidever, D. L., Majewski, S. R., & Patterson, R. J. 2006, *ApJ*, 650, L51
- Newberg, H. J., Willett, B. A., Yanny, B., & Xu, Y. 2010, *ApJ*, 711, 32
- Newberg, H. J., Yanny, B., Cole, N., Beers, T. C., Re Fiorentin, P., Schneider, D. P., & Wilhelm, R. 2007, *ApJ*, 668, 221
- Newberg, H. J., Yanny, B., Rockosi, C., et al. 2002, *ApJ*, 569, 245
- . 2003, *ApJ*, 596, L191
- Norris, J. E., Wyse, R. F. G., Gilmore, G., et al. 2010, *ApJ*, 723, 1632
- Peterson, R. C., Olszewski, E. W., & Aaronson, M. 1986, *ApJ*, 307, 139
- Prior, S. L., Da Costa, G. S., Keller, S. C., & Murphy, S. J. 2009, *ApJ*, 691, 306
- Robin, A. C., Reylé, C., Derrière, S., & Picaud, S. 2003, *A&A*, 409, 523
- Rocha-Pinto, H. J. 2010, in *IAU Symposium*, Vol. 265, *IAU Symposium*, ed. K. Cunha, M. Spite, & B. Barbuy, 255–262
- Schiavon, R. P. 2007, *ApJS*, 171, 146
- Schlegel, D. J., Finkbeiner, D. P., & Davis, M. 1998, *ApJ*, 500, 525
- Seares, F. H., Kapteyn, J. C., van Rhijn, P. J., Joyner, M. C., & Richmond, M. L. 1930, *Mount Wilson catalogue of photographic magnitudes in selected areas 1-139* (Carnegie institution of Washington)
- Searle, L., & Zinn, R. 1978, *ApJ*, 225, 357

- Sesar, B., Vivas, A. K., Duffau, S., & Ivezić, Ž. 2010a, *ApJ*, 717, 133
- Sesar, B., Ivezić, Ž, Lupton, R. H., et al. 2007, *AJ*, 134, 2236
- . 2010b, *ApJ*, 708, 717
- Sharma, S., Johnston, K. V., Majewski, S. R., Muñoz, R. R., Carlberg, J. K., & Bullock, J. 2010, *ApJ*, 722, 750
- Simon, J. D., & Geha, M. 2007, *ApJ*, 670, 313
- Simon, J. D., Geha, M., Minor, Q. E., et al. 2011, *ApJ*, 733, 46
- Suntzeff, N. B., Kraft, R. P., & Kinman, T. D. 1988, *AJ*, 95, 91
- Teuben, P. 1995, in *Astronomical Society of the Pacific Conference Series*, Vol. 77, *Astronomical Data Analysis Software and Systems IV*, ed. R. A. Shaw, H. E. Payne, & J. J. E. Hayes, 398–+
- Tonry, J., & Davis, M. 1979, *AJ*, 84, 1511
- van den Bergh, S. 2007, *AJ*, 134, 344
- van den Bergh, S., & Mackey, A. D. 2004, *MNRAS*, 354, 713
- Vivas, A. K., Jaffé, Y. L., Zinn, R., Winnick, R., Duffau, S., & Mateu, C. 2008, *AJ*, 136, 1645
- Vivas, A. K., & Zinn, R. 2003, *Mem. Soc. Astron. Italiana*, 74, 928
- . 2006, *AJ*, 132, 714
- Vivas, A. K., Zinn, R., Andrews, P., et al. 2001, *ApJ*, 554, L33
- . 2004, *AJ*, 127, 1158
- Vogt, S. S., Mateo, M., Olszewski, E. W., & Keane, M. J. 1995, *AJ*, 109, 151
- Walker, M. G., Mateo, M., Olszewski, E. W., Peñarrubia, J., Wyn Evans, N., & Gilmore, G. 2009, *ApJ*, 704, 1274
- Watkins, L. L., Evans, N. W., Belokurov, V., et al. 2009, *MNRAS*, 398, 1757
- Willett, B. A., Newberg, H. J., Zhang, H., Yanny, B., & Beers, T. C. 2009, *ApJ*, 697, 207
- Wolf, J., Martinez, G. D., Bullock, J. S., Kaplinghat, M., Geha, M., Muñoz, R. R., Simon, J. D., & Avedo, F. F. 2010, *MNRAS*, 406, 1220
- Worthey, G., Faber, S. M., Gonzalez, J. J., & Burstein, D. 1994, *ApJS*, 94, 687

Table 2: Adopted Positions and Weighted Mean Kinematics of 16 Virgo Substructure Candidates

Parameter	Value
RA ($^{\circ}$)	178.749
Dec ($^{\circ}$)	-0.586
l ($^{\circ}$)	274.557
b ($^{\circ}$)	59.118
distance (kpc)	14 ± 3
$\mu_{\alpha} \cos \delta$ (mas yr $^{-1}$)	-5.24 ± 0.43
μ_{δ} (mas yr $^{-1}$)	-0.91 ± 0.46
V_{GSR} (km s $^{-1}$)	152.6 ± 22.0^a
[Fe/H]	-1.1

^aThe V_{GSR} value quoted here is the weighted mean of 13 stars, after excluding the 3 likely RR Lyrae at $g \sim 17$. However, we note that if these candidate RR Lyrae stars have any large-amplitude RV variability, it seems to have no impact on our mean kinematics – including all 16 stars yields $V_{\text{GSR}} = 151.8 \pm 20.4$ km s $^{-1}$.